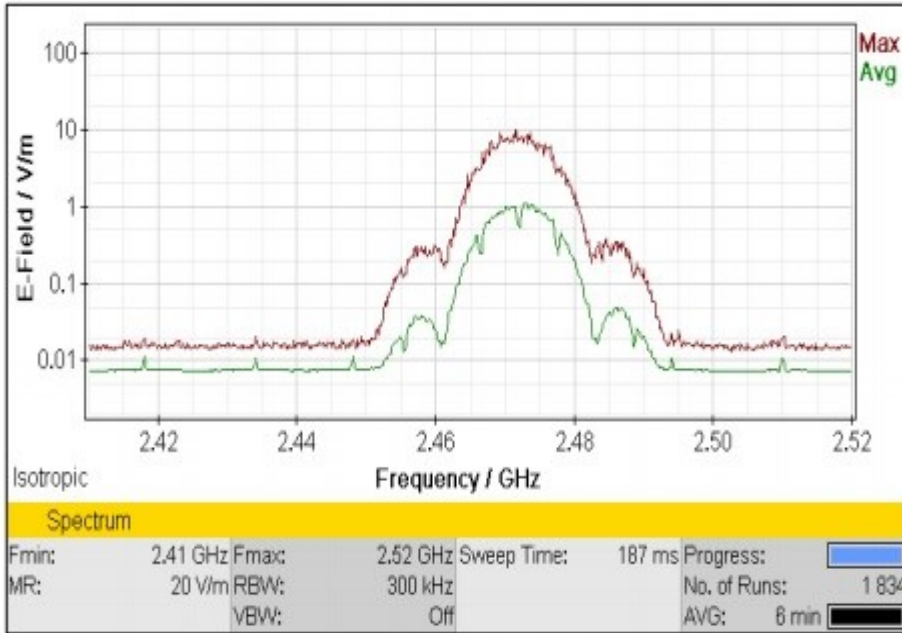


# Turkish Journal of Electromechanics & Energy

*an international open access journal*



[www.scienceliterature.com](http://www.scienceliterature.com)



# TURKISH JOURNAL OF ELECTROMECHANICS AND ENERGY VOLUME 1 NO 2

ISSN 2547-975X

2016 July-December Issue

Editors-in-Chief

- Dr. Mustafa Ergin Şahin, Recep Tayyip Erdoğan University, Turkey
- Dr. Ömer Necati Cora, Karadeniz Technical University, Turkey

Editorial Board

- Prof. Adel M. Sharaf, Sharaf Energy Systems, Canada
- Prof. Dina Simunic, University of Zagreb, Croatia
- Prof. Djamila REKIOUA, University of Bejaia, Algeria
- Prof. Halil İbrahim Okumuş, Karadeniz Technical University, Turkey
- Prof. Mitra Djamal, Institute Technology of Bandung (ITB), Indonesia
- Prof. Muammer Koç, HBKU, Qatar Foundation, Education City, Doha, Qatar
- Prof. Yaşar Demirel, University of Nebraska – Lincoln, United States
- Prof. Youcef Soufi, University of Tebessa-Algeria, Algeria
- Dr. Fareeha Zafar, Government College University Lahore, Pakistan
- Dr. Eyüp Fahri Keskenler, Recep Tayyip Erdoğan University, Turkey

Honorary Editors

- Prof. Hasan Karabulut, Recep Tayyip Erdoğan University, Turkey

**Lubricated Friction and Wear  
Properties of Ternary Zn-15Al-(1-  
5)Cu Alloys**

**Ali Paşa Hekimoğlu, Temel  
Savaşkan**  
1-7

**A Novel Regulation Inter-  
Coupled Control Scheme for  
Doubly Fed Wind Induction  
System**

**Sayed Osman Madbouly, Adel  
Mahmoud Sharaf**  
8-16

**Electromagnetic Radiation  
Measurement of a High Gain  
Wireless Network Adapter**

**Yasin Karan, Nilüfer As**  
17-23

**SCIENCE  
LITERATURE**

Kazım Karabekir Work-Center,  
F:3/C/196, 50. Year Street,  
Lalapaşa Neighborhood,  
Yakutiye, Erzurum, Turkey

<https://www.scienceliterature.com>

01.12.2016

# Lubricated friction and wear properties of Zn-15Al-(1-5)Cu Alloys

Ali P. Hekimoğlu<sup>1\*</sup>, T. Savaşkan<sup>2</sup><sup>1</sup> Department of Mechanical Engineering, Recep Tayyip Erdoğan University, Rize, Turkey<sup>2</sup> Department of Mechanical Engineering, Karadeniz Technical University, Trabzon, Turkey

Received: 9 August 2016; Revised: 21 September 2016; Accepted: 30 September 2016; Published: 1 December 2016

Turk J Electrom Energ Vol.: 1 No: 2 Page: 1-7 (2016)

SLOI: <http://www.sloi.org/>\*Correspondence E-mail: [ali.hekimoglu@erdogan.edu.tr](mailto:ali.hekimoglu@erdogan.edu.tr)

**ABSTRACT** In this study, lubricated friction and wear properties of Zn-15Al-(1-5)Cu alloys were investigated using a block-on-disc type test machine. Friction and wear tests were carried out at an oil flow rate of  $1 \text{ cm}^3 \text{ h}^{-1}$ , a sliding speed of  $2 \text{ m s}^{-1}$  and a contact pressure of 6 MPa for a sliding distance of 108 km. The variations in the friction coefficient, working temperature and wear volume of the alloys with sliding distance and copper content were monitored. The friction coefficient and the working temperature of the alloys became almost constant after the sliding distance of approximately 20 km, following an initial decrease. The wear volume of the alloys increased with increasing sliding distance and became almost constant after a sliding distance of 60 km. Zn-15Al-3Cu alloy exhibited the lowest friction coefficient, working temperature and wear volume among the alloys investigated. These observations are discussed in terms of the microstructural and mechanical properties of the alloys.

**Keyword:** Zn-15Al-Cu alloys; Lubricated friction and wear; Friction coefficient and wear volume; Wear surface

**Cite this article:** A.P. Hekimoğlu, T. Savaşkan, Lubricated friction and wear properties of Zn-15Al-(1-5)Cu Alloys, *Turkish Journal of Electromechanics & Energy* 1(2) 1-7 (2016)

## 1. INTRODUCTION

Zinc-based commercial alloys named as Zamak series were first developed in the 1920s and used successfully in some industrial applications [1-3]. Alzen alloys containing 30% Al (Alzen 305) and 50% Al (Alzen 501) were developed for bearing applications during World War II [3, 4]. Further research and development studies on the zinc-based alloys resulted in the development of ZA-8, ZA-12, and ZA-27 alloys containing 8, 12, and 27 % aluminium, respectively [1, 3, 4]. These studies showed that zinc alloys have a number of advantages over traditional bearing alloys including bronzes, brasses and cast irons [1-7]. The most important advantages of these alloys can be stated as high specific strength, good castability, easy machinability, low production energy and cost, excellent tribological and mechanical properties, good surface finishing and quality, superior embeddability and damping properties, and lower friction coefficient [1-7]. Lower friction coefficient, higher hardness and

high strength provide energy saving and longevity in engineering applications. Studies on the structure and properties of zinc-based alloys have been continued to improve their mechanical and tribological properties for some engineering applications [5, 8-9].

According to binary Al-Zn phase diagram [10-12] zinc-based alloys can be classified as eutectic (Zn-5Al), eutectoid (Zn-22Al) and monotectoid (Zn-40Al) alloys. Monotectoid Zn-Al alloys have been shown to be harder, stronger and more wear resistant than either eutectoid or eutectic ones [13]. However, hypereutectoid and eutectic Zn-Al based alloys have comparatively higher ductility, damping capacity and better castability [13]. Research works carried out on these alloys have been focused on the near eutectoid and monotectoid compositions and resulted in development of Zn-25Al-3Cu, Zn-27Al-2Cu, Zn-40Al-2Cu and Zn-40Al-3Cu alloys [8, 13-16]. However, the studies on the microstructure and properties of these alloys have been continued.

The studies on the zinc-based alloys have shown that the alloying elements including aluminium, copper and silicon have strong effects on their mechanical and tribological properties [10-19]. These effects have been attributed to the changes in their microstructures [13-21]. It has been observed that the addition of copper more than 2-3 % results in the formation of a metastable intermetallic phase called  $\epsilon$  ( $\text{CuZn}_4$ ) in the microstructure of the zinc-based alloys [14, 17-19]. This phase ( $\epsilon$ ) improves the load bearing capacity of these alloys by increasing their hardness, but decreases their strength and ductility [5, 6, 14, 17-19]. Furthermore, it ( $\epsilon$ ) causes a considerable amount of dimensional instability in these alloys [5, 6, 14, 17-19]. Therefore, the copper content should be taken as an important parameter in designing the zinc-based alloys for engineering applications.

Extensive research carried out recently on the high-zinc containing alloys resulted in the development of new Zn-15Al-based alloys for tribological applications [13, 14, 19]. The effect of copper content on the mechanical and dry wear properties of these alloys have been determined [13, 19, 20]. However, there is no information available about the effects of copper content on the lubricated friction and wear properties of these alloys. Therefore, the aim of this work is to investigate the effects of copper additions on the lubricated friction and wear properties of Zn-15Al alloy and determine the most suitable alloy composition for tribological applications.

## 2. EXPERIMENTAL PROCEDURE

Five (Zn-15Al-Cu) alloys were prepared by permanent mold casting using high purity aluminum (99.70 wt.%), zinc (99.90 wt.%) and copper (99.90 wt.%). The alloys were melted in an electric furnace and poured into a steel mold at temperatures of between 650 and 700 °C. The chemical composition analysis of the tested alloys was carried out by atomic absorption method. Their densities were determined by Archimedes' method. Metallographic investigations were performed with standard techniques and the samples etched in 1-4 % Nital. Microstructures of the alloys were examined using both optical and scanning electron microscopy (SEM).

The hardness of the alloys was measured using the Rockwell hardness F scale. Tensile tests were performed with the alloy samples having the diameter and gauge length of  $8 \times 40$  mm at a strain rate of  $6.25 \times 10^{-3} \text{ s}^{-1}$ . At least three measurements were taken to determine the hardness and tensile strength of the alloys.

Lubricated friction and wear properties of the experimental alloys were investigated using a block-on-disc type test machine. The schematic illustration of this test machine is shown in Fig. 1. The details of the friction-wear test machine and test sample were given elsewhere [20]. Friction and wear properties of the alloys were studied at a constant pressure of 6 MPa, a sliding speed of  $2 \text{ m s}^{-1}$ , oil flow rate of  $1 \text{ cm}^3 \text{ h}^{-1}$ , and a

sliding distance of 108 km for each samples. The tests were performed at room temperature ( $23 \pm 2$  °C) in air with a relative humidity of  $70 \pm 5\%$ . The temperature of the wear sample was monitored by inserting a copper-nickel thermocouple in a hole at a distance of 1.5 mm from the contacting surface. Each wear sample was ultrasonically cleaned and weighed before the tests using an electronic balance with an accuracy of 0.01 mg. The disc surface was cleaned with organic solvents to remove surface contaminants before each test. The samples cleaned in solvents and weighed to determine the mass loss after each test. Since the wear volume is a more meaningful parameter than the mass loss of the sliding bearings, the measured values of mass loss for the samples were converted into volume loss using the measured density of the alloys. The surface features and the subsurface microstructures of the wear samples were studied using SEM.

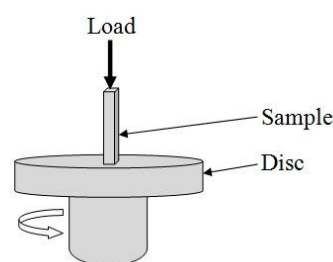


Fig. 1. Schematic illustration of the wear test machine

## 3. RESULTS

The chemical compositions of the experimental alloys are given in Table 1. The micrographs showing the microstructures of the Zn-15Al-Cu alloys are given in Figs. 2a-c. The microstructures of the alloys containing less than 2% copper consisted of partially decomposed proeutectic  $\beta$  dendrites, and  $\alpha$  and  $\eta$  phases as seen in Fig. 2a. It was observed that when the copper content exceeds 2-3%, copper rich  $\epsilon$  phase forms in the interdendritic regions and the volume fraction of this phase increases with increasing copper content, Fig. 2b and c.

Table 1. Chemical composition of the experimental alloys

Alloy	Chemical composition (wt. %)		
	Zn	Al	Cu
Zn-15Al-1Cu	84.2	14.9	0.9
Zn-15Al-2Cu	82.9	15.0	2.1
Zn-15Al-3Cu	81.9	15.2	2.9
Zn-15Al-4Cu	81.3	14.8	3.9
Zn-15Al-5Cu	80.4	14.8	4.8

The curves showing the changes in the tensile strength, hardness, yield strength, and elongation to fracture of the Zn-15Al-Cu alloys with copper content are given in Figure 3. The hardness, tensile strength, and yield strength of the alloys increased with increasing

copper content, but above 3% Cu the yield and tensile strength decreased. Elongation to fracture of the alloys decreased with increasing copper content, Figure 3.

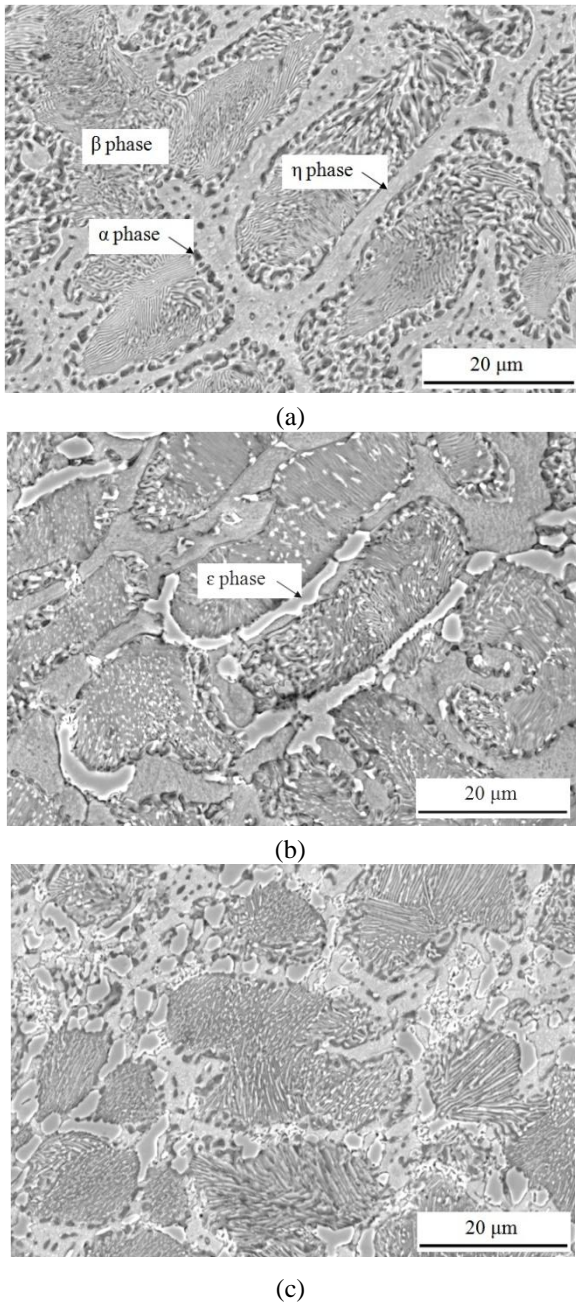


Fig. 2. SEM micrographs of the microstructure of (a) Zn-15Al-1Cu, (b) Zn-15Al-3Cu and (c) Zn-15Al-5Cu alloys

The changes in friction coefficient, working temperature, and wear volume of the alloys as a function of sliding distance and copper content are shown in Figs. 4, 5 and 6, respectively. The friction coefficient of the experimental alloys reached steady states after showing a sharp decrease with sliding distance, Fig. 4a and b. However, the working temperature of the alloys reached steady states after showing a sharp increase and a decrease as seen in Fig. 5a, and b. The wear volume of the alloys increased with

increasing sliding distance and reached almost a constant value after the 60 km, Fig. 6. The friction coefficient, working temperature and wear volume of the alloys decreased with increasing copper content, but above 2-3% Cu the trend reversed, Fig. 7.

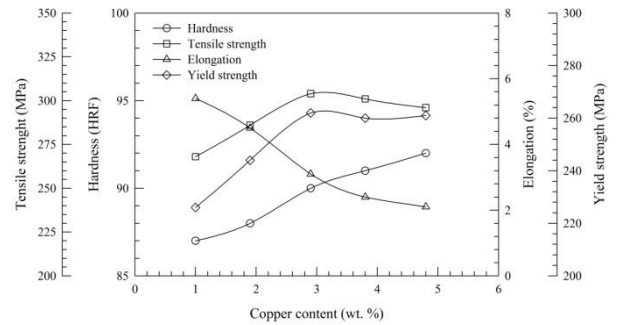


Fig. 3. The curves showing the changes in tensile strength, hardness, elongation, and yield strength of Zn-15Al-Cu alloys with their copper content

Smearing and scratches were observed to be the main surface features of the wear samples of the experimental alloys as seen in Figs. 8a-c. As the copper content increased the amount of smeared material on their wear surfaces decreased, but the number and size of the scratches increased as it can be noticed from Figure 8a and 8c.

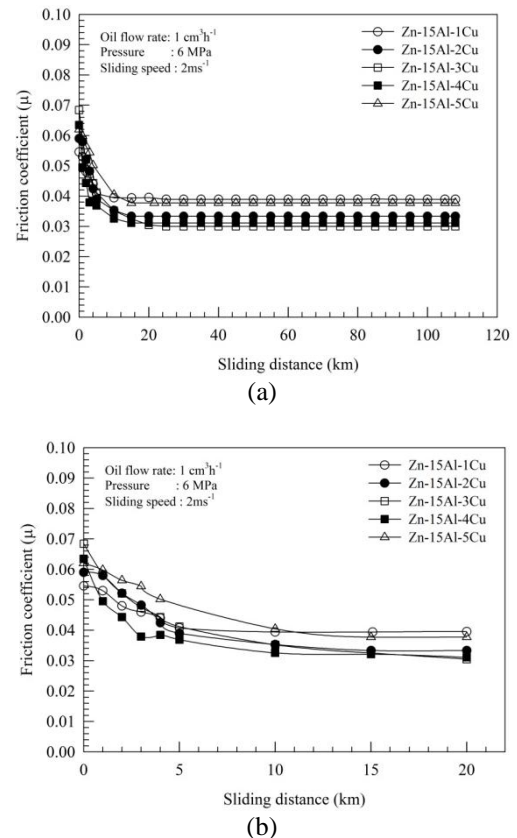


Fig. 4. The curves showing the changes in friction coefficient of Zn-15Al-(1-5)Cu alloys for the sliding distances of (a) 108 and (b) 20 km

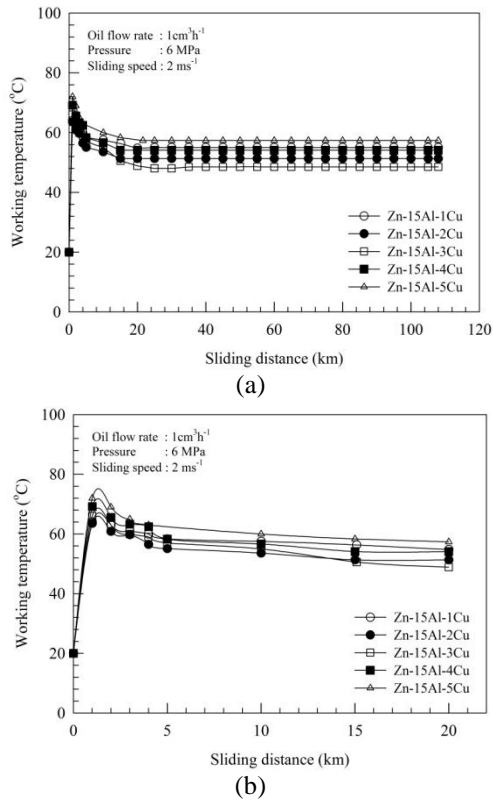


Fig. 5. The curves showing the changes in working temperature of Zn-15Al-(1-5)Cu alloys for the sliding distances of (a) 108 and (b) 20 km

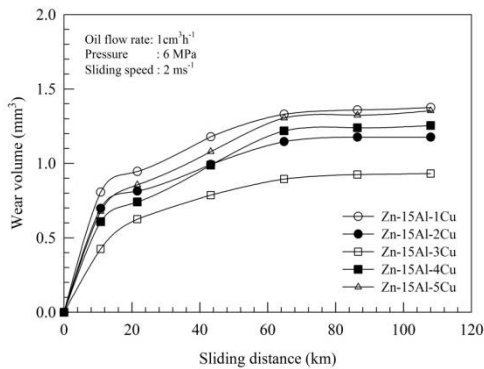


Fig. 6. The curves showing the changes in wear volume of the Zn-15Al-(1-5)Cu alloys as a function of sliding distance

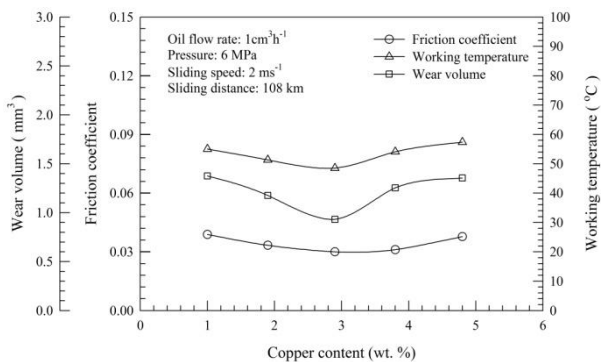
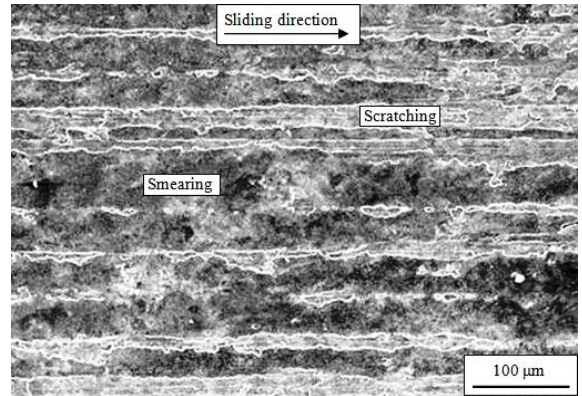
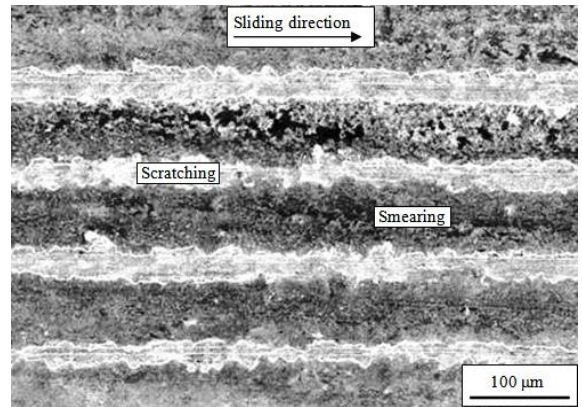


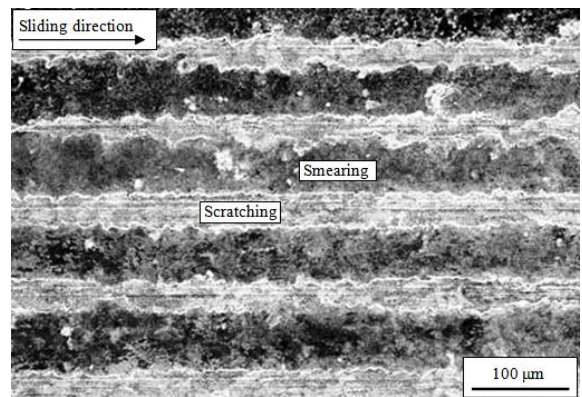
Fig. 7. The curves showing the variations in the friction coefficient, working temperature, and wear volume of the Zn-15Al-(1-5)Cu alloys with copper content



(a)



(b)



(c)

Fig. 8. SEM micrograph showing the wear surfaces of (a) Zn-15Al-1Cu, (b) Zn-15Al-3Cu and (c) Zn-15Al-5Cu alloys

#### 4. DISCUSSION

The microstructure of the Zn-15Al-1Cu alloys consisted of  $\beta$  dendrites and  $\alpha$  and  $\eta$  phases as seen Fig.2a. The  $\epsilon$  ( $\text{CuZn}_4$ ) phase formed in the microstructure of the alloys when their copper content exceeded 2%, and the volume fraction of this phase increased with increasing copper content as seen in Figs. 2a and b. This observation is in agreement with the results of previously published papers [20-23]. Formation of these phases can be related to the phase

transformations which take place during solidification of Zn-15Al based alloys [19].

The hardness, tensile, and yield strength of the experimental alloys increased with increasing copper content; but above 3% Cu, the yield and tensile strength decreased. Elongation to fracture of the alloys decreased with increasing copper content (Figure 3). These observations can be attributed to the solid solution hardening and formation of the relatively hard and brittle copper-rich intermetallic  $\epsilon$  phase in the alloys containing more than 2% Cu [17-20].

The friction coefficient of the experimental alloys decreased with increasing sliding distance and became almost constant (Fig. 4a and b). The working temperature of these alloys also became almost constant, but after showing a sharp increase and a decrease (Fig. 5a and b). These observations may be related to metal-to-metal contact due to inadequate oil film on the mating surfaces. Metal-to-metal contact gives rise to high friction force which results in high friction coefficient [22-24]. It is well known that the friction coefficient of the lubricated systems decreases with increasing oil film thickness and when the oil film thickness becomes sufficient to separate the rubbing surfaces friction coefficient levels off and becomes almost constant [22-24]. Working temperature of the alloys showed a similar trend with their friction coefficient. This can be attributed to the frictional heat caused by rubbing of the surfaces.

The wear volume of the alloys increased with increasing sliding distance and reached almost a constant value after 60 km, Fig. 6c. This can be attributed to the increase in the oil film thickness with sliding distance as was mentioned in the discussion of the friction coefficient of these alloys.

The friction coefficient, working temperature and wear volume of the alloys decreased with increasing copper content, but above 3% Cu the trend reversed, Fig. 7. These observations can be explained in terms of the microstructure and tensile strength of the alloys. It is known that as the copper content increases the hardness of the alloys increase, but their elongation to fracture decreases. Tensile strength of these alloys also increases with increasing copper content up to 3%, but above this level the trend reverses. It is also known that when the copper content of the Zn-Al-Cu alloys exceeds 2-3%, a hard and brittle  $\epsilon$ -phase form in their microstructures and the volume fraction of this phase increases with increasing copper content [17-20]. Therefore, the changes in the tensile strength of the Zn-15Al-Cu alloys can be attributed to the solid solution strengthening and cracking tendency, respectively [17-20]. According to the adhesive wear law, the friction coefficient and wear volume of the materials decrease as their hardness and strength increase [22, 25, 26]. Therefore, the friction coefficient, working temperature and wear volume of these alloys are expected to decrease with copper content up to 3%. The increase in these parameters may be related to the formation of hard and brittle  $\epsilon$ -phase and a reduction in the tensile strength of the alloys when

their copper content exceeds 3%. This is because the tensile strength of the zinc-based alloys is more influential on their wear volume than their hardness [20]. It is also known that there is a strong relationship between the wear resistance and the tensile strength of Zn-Al-Cu alloys [17, 18, 20]. Therefore, the alloys which have the highest tensile strength are expected to show the highest wear resistance or the lowest wear volume.

Smearing and scratches were observed to be the main features of the worn surface of the alloy samples, Fig. 8a and b. Smearing takes place by back transferring of the wear debris from the disc to the sample surface; scratches occur due to the removal of hard silicon and  $\epsilon$  particles from the wear surface of the samples and microcracks result from the brittleness of the hard surface layer as reported in previously published papers [17, 18, 20-22].

## 5. CONCLUSIONS

1. Microstructure of Zn-15Al-(1-5)Cu alloys consists of  $\alpha$ ,  $\beta$  and  $\eta$  phases. When the copper content exceeds 2%, copper rich  $\epsilon$  phase forms in the microstructure.
2. Hardness of Zn-15Al-(1-5)Cu alloys increase with increasing copper content. Their tensile strength also increase with increasing copper content, but the trend reverses above 3% Cu.
3. Zn-15Al-3Cu alloy exhibits the lowest friction coefficient, working temperature and wear volume among Zn-15Al-(1-5)Cu alloys.
4. The friction coefficient and working temperature of Zn-15Al-(1-5)Cu alloys decrease with increasing sliding distance, but above a sliding distance of approximately 20 km they become almost constant.
5. Wear surfaces of Zn-15Al-(1-5)Cu alloys are characterized by smearing and scratches.

## Acknowledgement

This work was supported by the Karadeniz Technical University under a research contract (No. 2008.112.03.2).

## References

- [1] F.E. Goodwin, A.L. Ponikvar, Engineering Properties of Zinc Alloys, International Lead Zinc Research Organization, Third Edition, USA, January, (1989).
- [2] E. Gervais, R.J. Barnhurst, C.A. Loong, An Analysis of Selected Properties of ZA Alloys, Journal of Metals, 37(11), 43-47, (1985).
- [3] A.F. Skenazi, J. Pelerin, D. Coutouradis, B. Magnus, M. Meeus, Some Recent Developments in the Improvement of the Mechanical Properties of Zinc Foundry Alloys, Metallwissenschaft und Technik, 37(9), 898-902, (1983).
- [4] E. Gervais, H. Levert, M. Bess, The Development of a Family of Zinc-Based Foundry Alloys, American Foundrymen's Society Transaction, 88, 183-194, (1980).

- [5] B.K. Prasad, Effects of Silicon Addition and Test Parameters on Sliding Wear Characteristics of Zinc-Based Alloy Containing 37.5% Aluminium, *Materials Transactions, JIM.*, 38(8), 701-706, (1997).
- [6] T. Savaşkan, Y. Alemdağ, Effects of Pressure and Sliding Speed on the Friction and Wear Properties of Al-40Zn-3Cu-2Si Alloy: A Comparative Study with SAE 65 Bronze, *Materials Science and Engineering A*, 496, 517-523, (2008).
- [7] P. Delneville, Tribological Behaviour of Zn-Al Alloys (ZA27) Compared with Bronze When Used as a Bearing Material with High Load and very Low Speed, *Wear*, 105, 283-292, (1985).
- [8] T. Savaşkan, S. Murphy, Mechanical Properties and Lubricated Wear of Zn-25 Al Based Alloys, *Wear*, 116, 221-224, (1987).
- [9] T. Calayag, D. Ferres, High-Performance, High-Aluminum Zinc Alloys for Low-Speed Bearings and Bushings, SAE Annual Conference, Paper No 820643, 2241-2251, (1983).
- [10] A.A. Presnyakov, Y.A. Gorban, V.V. Chrevyakova, The Aluminum-Zinc Phase Diagram, *Russian Journal of Physical Chemistry*, 35, 632-633 (1961).
- [11] H. Auer, K.E. Mann, Magnetische Untersuchung des Systems Zink-Aluminium, *Zeitschrift für Metallkunde*, 28, 323-326, (1936).
- [12] G.M. Kuznetsov, A.D. Barsukov, G.B. Krivosheeva, Calculation of Phase Equilibria of The Al-Zn System, *Russian Metall*, 5, 195-198, (1986).
- [13] A.P. Hekimoğlu, T. Savaşkan, Structure and mechanical properties of Zn-(5–25) Al alloys, *International Journal of Materials Research*, 105(11), 1084-1089, (2014)
- [14] T. Savaşkan, A.P. Hekimoğlu, Effect of quench-ageing treatment on the microstructure and properties of Zn-15Al-3Cu alloy, *International Journal of Materials Research*, 106(5), 481-487, (2015).
- [15] T. Savaşkan, R. Anvari, Friction and Wear Properties of Zn-25Al-Based Bearing Alloys, *Tribology Transactions*, 57(3), 435-444, (2014).
- [16] T. Savaşkan, O. Bican, Y. Alemdağ, Developing aluminium-zinc-based a new alloy for tribological applications, *Journal of Materials Science*, 44 (8), 1969-1976, (2009).
- [17] T. Savaşkan, A.P. Hekimoğlu, G. Pürçek, Effect of copper content on the mechanical and sliding wear properties of monotectoid-based zinc-aluminium-copper alloys, *Tribology International* 37(1), 45-50, (2004).
- [18] T. Savaşkan, G. Pürçek, A.P. Hekimoğlu, Effect of copper content on the mechanical and tribological properties of ZnAl27-based alloys, *Tribology Letters* 15(3), 257-263, (2003).
- [19] T. Savaşkan, A.P. Hekimoğlu, Microstructure and mechanical properties of Zn-15Al-based ternary and quaternary alloys, *Materials Science and Engineering: A* 603, 52-57, (2014).
- [20] T. Savaşkan, A.P. Hekimoğlu, Relationships between mechanical and tribological properties of Zn-15Al-based ternary and quaternary alloys, *International Journal of Materials Research* 107(7), 646-652, (2016).
- [21] A.P. Hekimoğlu, T. Savaşkan, Effects of Contact Pressure and Sliding Speed on Unlubricated Friction and Wear Properties of Zn-15Al-3Cu-1Si Alloy, *Tribology Transactions: 0(0)*, 1-8, (2016) Published Online, <http://dx.doi.org/10.1080/10402004.2016.1141443>.
- [22] J. Halling, Principles of Tribology, Macmillan Education Ltd., Great Britain, (1989).
- [23] T. Savaşkan, R.A. Maleki, H.O. Tan, Tribological properties of Zn-25Al-3Cu-1Si alloy, *Tribology International*, 81, 105-111, (2015).
- [24] F.P. Bowden, D. Tabor, The friction and lubrication (2nd ed.) Oxford university press, London, (1967).
- [25] I.M. Hutchings, Tribology: Friction and Wear of Engineering Materials, Edward Arnold, USA, (1992).
- [26] K.H. Zum Gahr, Microstructure and Wear of Materials, Elsevier, Oxford, (1987).

#### Biographies



**Ali Paşa HEKİMOĞLU**- Ali Paşa Hekimoğlu was born in Trabzon and graduated from Karadeniz Technical University (KTU) in 1997. He completed his MSc and PhD in Mechanical Engineering

Department of this University. He worked as a specialist at some Turkish Republic Ministries between 1998 and 2010 and participated in some European Commission Motor Vehicles Technical Committees as a member of Turkish Delegation. During these years, he prepared some projects and 2 investigative reports about Turkish Automotive Industry. Between 2004 and 2006, he attained European Union (EU) Policies and International Relations Training Programmes organized by Ankara University European Research Center and got a title of EU and international relations expert. In 2006, he was awarded with the Indian Government Scholarship in the scope of Indian-Turkish Economical Corporation Agreement and commissioned by the Turkish Government in the New Delhi. He was also granted due to his successful works by the minister and undersecretary in the Republic of Turkey Ministry of Industry and Trade. After 2010, he worked in Eastern Black Sea Development Agency on regional planning and development and he prepared many research and planning documents on regional industry of Eastern Black Sea Region of Turkey. He was participated in some training commissions of the chamber of mechanical engineers and gave a number of technical

seminars. Ali Paşa Hekimoğlu joined the Mechanical Engineering Department of Recep Tayyip Erdoğan University as an Assistant Professor in 2015. He has authored 8 peer reviewed scientific papers. He is conducting 4 research projects about new aluminium based alloys development and supervising 6 MSc students.

E-mail: [ali.hekimoglu@erdogan.edu.tr](mailto:ali.hekimoglu@erdogan.edu.tr)



**Temel SAVAŞKAN-** Temel

Savaşkan was born in Trabzon and worked as a Research Assistant at KTU between 1972 and 1974 after graduating from Ege (Aegean) University in 1970. He completed his MSc and PhD in Metallurgy and Materials Engineering Department of Aston University in 1975 and 1981, respectively. He worked as a Research Fellow at Marmara Research Institute of the Scientific and Technical Research Council of Turkey between 1981 and 1982. He also worked as a postdoctoral research fellow in Atlantic Industrial Research Institute and Metallurgical Engineering Department of Technical University of Nova Scotia in Canada between 1982 and 1986. He joined the Mechanical Engineering Department of Karadeniz Technical University (KTU) as an Assistant Professor in 1986. He became an Associate Professor in 1987 and was appointed as a full Professor in 1993 in the same department. Professor Temel Savaskan worked as the Director of Graduate School of Natural and Applied Sciences between 1989 and 1995 and as the Vice Rector/President of KTU between 1996 and 1997. He also worked as the Director of Research and Development Center of Materials Sciences and Manufacturing Technologies between 1995 and 2005, as the Head of Mechanical Engineering Department between 1999 and 2005 of the same university, as a Member of the Certification Committee in Trabzon Regional Representative of the Turkish Standard Institution between 1996 and 2012 and as the Head of Materials Division of the Mechanical Engineering Department of KTU between 1997 and 2015. Professor Temel Savaşkan has authored more than 50 peer reviewed scientific papers and three text books, supervised 10 PhD and 18 MSc theses, and completed 17 scientific research project reports. He also reviewed a large number of scientific papers, project proposals and reports.

E-mail: [savaskan@ktu.edu.tr](mailto:savaskan@ktu.edu.tr)

# A Novel Regulation Inter-Coupled Control Scheme for Doubly Fed Wind Induction System

Sayed O. Madbouly<sup>1</sup>, Adel M. Sharaf<sup>2\*</sup>

<sup>1</sup>Electric Power and Machines Dept., Ain Shams University, Cairo, Egypt

<sup>2</sup>Sharaf Energy Systems, Inc., Fredericton-NB, Canada

Received: 07 July 2015; Revised: 31 July 2015; Accepted: 08 August 2016; Published: 1 December 2016

Turk J Electrom Energ Vol: 1 No: 2 Page: 8-16 (2016)

SLOI: <http://www.sloi.org/>

\*Correspondence E-mail: [profdramsharaf@yahoo.ca](mailto:profdramsharaf@yahoo.ca)

**ABSTRACT** The paper presents a novel variable structure coordinated controller for a brushless doubly fed induction generator (BDFG) to improve its dynamic performance. The system under study consists of a BDFG driven variable speed wind turbine. The machine model in d-q power winding (PW) synchronously rotating reference frame is formulated in Matlab/Simulink. The new vector control algorithm which contains two control paths was then developed. The first path controls the active power of the power winding and the other controls its reactive power. The dynamic performance of the BDFG with the new controller has been tested when the overall system is subjected to a various patterns of wind speed. Also the transient and dynamic response is tested under sudden short circuit and open circuit at the generator bus. The digital simulation results showed that the new vector controller improved the dynamic performance of the overall system.

**Keywords:** Wind-brushless doubly fed induction machine, Vector control, Variable structure coordinated controller

**Cite this article:** S.O. Madbouly, A.M. Sharaf, A Novel Regulation Inter-Coupled Control Scheme for Doubly Fed Wind Induction System, *Turkish Journal of Electromechanics & Energy* 1(2) 8-16 (2016)

## 1. INTRODUCTION

Recently, variable speeds doubly fed generators have been extensively utilized in wind energy applications. They provide the ability of adjusting the wind turbine speed as a function of wind speed in order to maximize the output power [1]. One of these generators is the Doubly Fed Induction Generator (DFIG) which allows the speed variation through the use of bi-directional power converter connected to its rotor [2]. The disadvantages of DFIG are the presence of slip rings and brushes, which need frequent inspections and maintenance. Therefore, the reliability of the overall system is decreased and the maintenance cost is increased [3].

Efforts have been directed towards eliminating the slip rings and brushes while maintaining the benefits of DFIG. In this paper Brushless Doubly Fed Induction Generator (BDFG) is proposed. The construction feature of grid connected BDFG is shown in Figure 1. In this configuration, the stator incorporates two sets of three phase windings with different number of poles. One of them is connected directly to the grid, and is called the Power Winding (PW), since it handles most of machine

power. The other one is connected via a bi-directional converter to the grid, it handles a small percentage of machine power and it is called the Control Winding (CW).

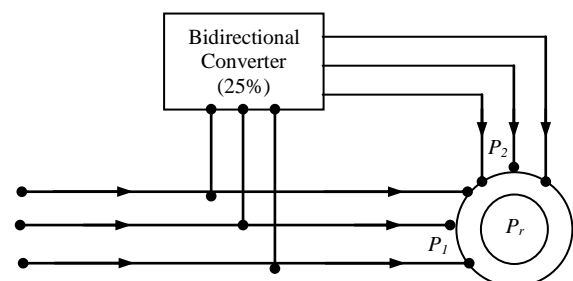


Fig. 1. Configuration of grid connected brushless doubly fed induction machine

The power rating of the converter depends on the adjustable speed range, which is limited in variable speed wind turbines. Therefore, the converter rating is a small percentage of the machine rating [4].

In BDFG the active and the reactive power of the power winding can be controlled through controlling the magnitude; frequency and phase sequence of the applied voltage of the control winding. This can be implemented by using direct torque control technique [5] or vector control schemes [3, 6, 7]. This paper presents a novel vector control of the BDFG which achieves an enhanced decoupled control of active and reactive power of BDFG driven variable speed wind turbine.

**2. SYSTEM MODELING**

The system model is consisting of three main parts.

*2.1 Wind Turbine Model*

The mechanical power output from the wind turbine can be calculated from the following equation:

$$P_m = \frac{1}{2} \rho \pi R_r^2 v_w^3 C_p(\beta, \lambda) \tag{1}$$

Where  $v_w$  is the wind speed,  $\rho$  is the air density,  $R_r$  is the radius of the turbine blades, and  $C_p$  is the power coefficient or performance coefficient which is a function of both the tip speed ratio  $\lambda$ , and the blade pitch angle  $\beta$ . The tip speed ratio  $\lambda$  (TSR) is the ratio between the tip speed and the wind speed. It can be expressed as follows [8, 9];

$$\lambda = \frac{\omega_r \cdot R_r}{v_w} \tag{2}$$

The relation between the power coefficient and both of the tip speed ratio  $\lambda$  and the pitch angle  $\beta$  is approximated by the following equation [10, 11].

$$C_p(\lambda, \beta) = 0.22 \left( \frac{116}{\lambda_i} - 0.4\beta - 5 \right) \cdot e^{-\frac{12.5}{\lambda_i}} \tag{3}$$

Where  $\lambda_i$  is given by:

$$\frac{1}{\lambda_i} = \frac{1}{\lambda + 0.08\beta} - \frac{0.035}{\beta^3 + 1} \tag{4}$$

Figure 2 shows the relation between the performance coefficient and the tip speed ratio at different pitch angle, it can be seen that the maximum performance coefficient is  $C_{pmax}=0.438$  and occurs at a tip speed ratio of  $\lambda_{opt}=6.3$ .

The wind turbine model can be simulated in Matlab/Simulink program as shown in Figure 3 [12, 13].

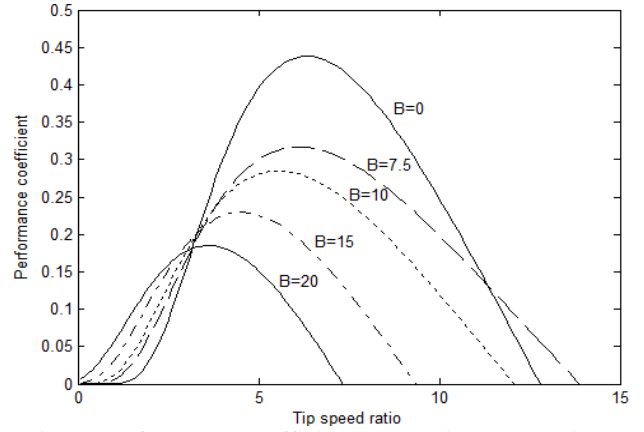


Fig. 2. Performance coefficient versus tip-speed ratio at different pitch angles

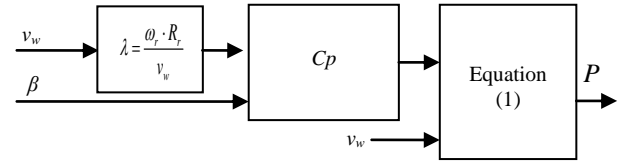


Fig. 3. Wind turbine input- output model

*2.2 Drive Train Model*

The drive train model of the wind turbine is represented by two mass models as shown in Figure 4. The model consists of two main masses, i.e. turbine mass and generator mass. The two masses are connected to each other with a shaft that has a stiffness constant ( $K_s$ ) and damping constant ( $D_s$ ). The input to the drive train model is the aerodynamic torque referred to the generator side (i.e. high speed side) and the output from the model is the generator speed ( $\omega_g$ ). The equations of the drive train are:

$$T_t - K_s \theta_{tg} - D_s \cdot (\omega_t - \omega_g) = J_t \cdot \frac{d\omega_t}{dt} \tag{5}$$

$$K_s \theta_{tg} + D_s \cdot (\omega_t - \omega_g) - T_g = J_g \cdot \frac{d\omega_g}{dt} \tag{6}$$

Where  $T_t$ ,  $J_t$  and  $\omega_t$  are the torque, inertia and speed of the wind turbine referred to the generator side, respectively;  $T_g$ ,  $J_g$  and  $\omega_g$  are the torque, inertia and speed of the generator, respectively; and  $\theta_{tg}$  is the shaft twist angle, which is given by:

$$\frac{d\theta_{tg}}{dt} = (\omega_t - \omega_g) \tag{7}$$

*2.3 Dynamic Model of BDFG*

In order to derive the model of BDFM, the following assumptions are made [14].

- Assume linear magnetic circuit, and neglect saturation.
- Sinusoidal distributed stator winding
- No direct mutual coupling between the power and control winding.

The BDFM equations are derived in the  $d$ - $q$  reference frame which rotates synchronously with the power

winding stator flux by angular speed of  $\omega_r$ (The d- axis is taken to be aligned with the PW flux space vector) [15, 16, 17]. These are:

$$v_p = R_{sp}i_p + \frac{d\psi_p}{dt} + j\omega_1\psi_p \quad (8)$$

$$\psi_p = L_{sp}i_p + L_{hp}i_r \quad (9)$$

$$v_c = R_{sc}i_c + \frac{d\psi_c}{dt} + j(\omega_1 - (p_1 + p_2)\omega_r)\psi_c \quad (10)$$

$$\psi_c = L_{sc}i_c + L_{hc}i_r \quad (11)$$

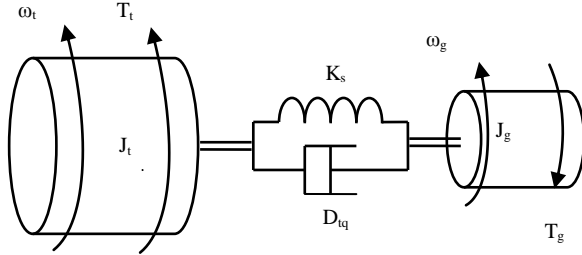


Fig. 4. Drive train model

$$v_r = R_r i_r + \frac{d\psi_r}{dt} + j(\omega_1 - p_1\omega_r)\psi_r \quad (12)$$

$$\psi_r = L_r i_r + L_{hp}i_p + L_{hc}i_c \quad (13)$$

Where:

- $v_p, v_c$  and  $v_r$  are the PW, CW and rotor winding voltage vector respectively.
- $R_{sp}, R_{sc}$  and  $R_r$  are the PW, CW and rotor resistances.
- $L_{sp}, L_{sc}$  and  $L_r$  are the self-inductances of the PW, CW and rotor winding respectively.
- $L_{hp}$  is the mutual inductance between the PW and the rotor winding and  $L_{hc}$  is the mutual inductance between the CW and the rotor winding.
- $\psi_p, \psi_c$  and  $\psi_r$  are the PW, CW and rotor flux space vectors respectively.

The electromagnetic torque can be expressed as the sum of the electromagnetic torques produced by the PW and CW. It can be expressed by the following equation.

$$T_{em} = \frac{3}{2} p_1 \text{Im}[i_p \psi_p^*] + \frac{3}{2} p_2 \text{Im}[i_c \psi_p^*] \quad (14)$$

The power windings active and reactive powers are expressed as:

$$P_p = \frac{3}{2} (v_{pd}i_{pd} + v_{pq}i_{pq}) \quad (15)$$

$$Q_p = \frac{3}{2} (v_{pq}i_{pd} - v_{pd}i_{pq}) \quad (16)$$

### 3. CONTROL STRATEGY OF THE ALL SYSTEM

The control strategy of the overall system can be divided into two parts as following.

#### 3.1 Generator Control Part

The target of this part is to achieve a fully independent control of the active and reactive power of the PW, through the control of the control winding

voltage. This can be fulfilled using the vector control technique as described in the following section.

#### 3.2 PW Power Control

The model of the BDFG is derived in the PW synchronously rotating  $d$ - $q$  reference frame with the  $d$ -axis aligned with the PW flux. Accordingly,  $\psi_{pd} = |\psi_p|$  and there is no component in the  $q$ -axis:

$$\psi_{pq} = 0 \quad \& \quad \psi_{pd} = |\psi_p| \quad (17)$$

Since the PW is connected directly to the grid,  $|\psi_p|$  and  $v_{pd}$  can be considered constant. Consequently, equations (12) and (13) can be simplified as follows:

$$p_p = \frac{3}{2} v_{pq} i_{pq} \quad \text{and} \quad Q_p = \frac{3}{2} v_{pd} i_{pd} \quad (18)$$

It can be seen from (18) that the active and reactive power can be regulated by the  $q$ -component and  $d$ -component of the PW current respectively

#### 3.2.1 PW Current Control

The dynamic relation between the CW and the PW currents is derived in Appendix (A).

$$\frac{di_{cd}}{dt} = \frac{R_r L_{sp}}{L_{hp} L_{hc}} i_{pd} + \frac{\sigma L_r L_{sp}}{L_{hp} L_{hc}} \frac{di_{pd}}{dt} - \frac{R_r}{L_{hp} L_{hc}} |\psi_p| - \frac{\sigma L_r L_{sp} \omega_{sl}}{L_{hp} L_{hc}} i_{pq} + \omega_{sl} i_{cq} \quad (19)$$

$$\frac{di_{cq}}{dt} = \frac{R_r L_{sp}}{L_{hp} L_{hc}} i_{pq} + \frac{\sigma L_r L_{sp}}{L_{hp} L_{hc}} \frac{di_{pq}}{dt} - \frac{L_r \omega_{sl}}{L_{hp} L_{hc}} |\psi_p| + \frac{\sigma L_r L_{sp} \omega_{sl}}{L_{hp} L_{hc}} i_{pd} - \omega_{sl} i_{cd} \quad (20)$$

where;

$$\omega_{sl} = \omega_1 - p_1 \omega_r \quad (21)$$

The first two terms of (19) and (20) represent the direct relation between ( $i_{pd}$  and  $i_{cd}$ ) and ( $i_{pq}$  and  $i_{cq}$ ), respectively while the other terms represent the cross coupling terms which cross couple the  $d$  and  $q$  axis variables (i.e. changing the CW current in one axis affects the PW current not only in this axis but also in the other axis). From (19) and (20) it can be seen that, the PW currents ( $i_{pd}$  and  $i_{pq}$ ) can be linearly controlled by the CW currents ( $i_{cd}$  and  $i_{cq}$ ) respectively after compensating the cross coupling terms by feed forward control action.

#### 3.3 Control of CW Currents

From (8) to (16), the dynamic relation between the CW current and the CW voltage in the  $d$ -axis ( $v_{cd}$  and  $i_{cd}$ ) and  $q$ -axis ( $v_{cq}$  and  $i_{cq}$ ) can be obtained as follows:

$$V_{cq} = R_{sc} i_{cq} + (L_{sc} - \frac{L_{hc}^2}{\sigma L_r}) \frac{di_{cq}}{dt} + \frac{R_r L_{sp} L_{hc}}{\sigma L_{hp} L_r} i_{pq} + [\omega_{sl} (L_{sc} - \frac{L_{hc}^2}{\sigma L_r}) - p_2 L_{sc} \omega_r] i_{cd} + p_2 \omega_r \frac{L_{sp} L_{hc}}{L_{hp}} i_{pd} + \frac{L_{hc}}{L_{hp}} \left( \frac{\omega_{sl} (\sigma - 1)}{\sigma} - p_2 \omega_r \right) |\psi_p| \quad (22)$$

$$V_{cd} = R_{sc} i_{cd} + (L_{sc} - \frac{L_{hc}^2}{\sigma L_r}) \frac{di_{cd}}{dt} + \frac{R_r L_{sp} L_{hc}}{\sigma L_{hp} L_r} i_{pd} - [\omega_{sl} (L_{sc} - \frac{L_{hc}^2}{\sigma L_r}) - p_2 L_{sc} \omega_r] i_{cq} - p_2 \omega_r \frac{L_{sp} L_{hc}}{L_{hp}} i_{pq} - \frac{R_r L_{hc}}{\sigma L_{hp} L_r} |\psi_p| \quad (23)$$

Similar to (19) and (20), it can be seen that the first two terms in (22) and (23) define the direct relation between ( $v_{cd}$  and  $i_{cd}$ ) and ( $v_{cq}$  and  $i_{cq}$ ) respectively. From this relation, it can be seen that, the CW currents ( $i_{cd}$  and  $i_{cq}$ ) can be linearly controlled by the CW voltages ( $v_{cd}$

and  $v_{cq}$ ) respectively. The other terms in (22) and (23) (from the 3<sup>rd</sup> term up to the 6<sup>th</sup> term) represent the cross coupling disturbances between the d and q axes.

### 3.4 The Proposed Control Scheme

From the previous analysis, the active power of the PW can be controlled by the q-component of the CW voltage, while the reactive power can be controlled by the d-component of the CW voltage as follows:

$$\begin{aligned}
 P_{pw} &\xrightarrow{\text{Controlled}} i_{pq} \xrightarrow{\text{Controlled}} i_{cq} \xrightarrow{\text{Controlled}} v_{cq} \\
 Q_{pw} &\xrightarrow{\text{Controlled}} i_{pd} \xrightarrow{\text{Controlled}} i_{cd} \xrightarrow{\text{Controlled}} v_{cd}
 \end{aligned}$$

The novel controller developed by the second author is a variable structure sliding mode VSC-SMC controller with dual loop inter-coupling of the powers  $P, Q$  tracking loops as shown in Figure 5. The selected (d-q) current references are later input to classical PI inner controllers to derive the d-q command voltages ( $v_{cd}^*, v_{cq}^*$ ) as shown in Figure 6. The use of variable structure outer controller for ( $P_{ref}, Q_{ref}$ ) control loops ensure fast dynamic reference and minimal ripple content due to the insertion of the low pass filter to ( $\sigma_p, \sigma_q$ ) sliding surface slopes.

### 3.5 Wind Turbine Control Scheme

The target from variable speed wind turbine controller is to maximize the captured power from the wind when the wind speeds below its rated value and limiting the output power at the rated value when the wind speed exceeds its rated value. Two controllers are required to satisfy the previous control strategy.

### 3.6 Speed Controller

Figure 6 shows the speed controller that the reference speed is compared with the actual speed to get the speed error which is manipulated by a PI controller. The output from the PI controller is the reference active power, which is used by the BDFG controller as mentioned before. The reference speed is determined from the maximum power point tracking curve shown in Figure 7.

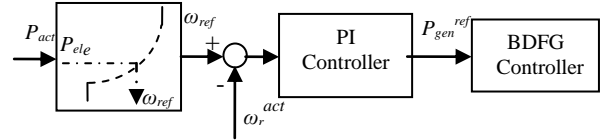


Fig. 6. Block diagram of speed controller

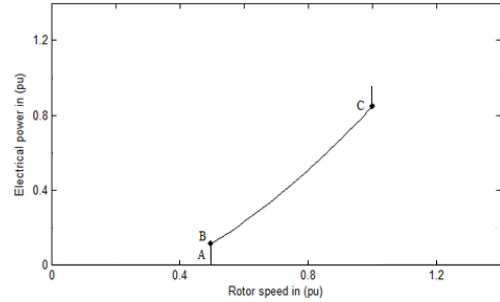


Fig. 7. Optimal output power versus rotor speed

### 3.7 Pitch Angle Controller

The pitch angle controller is only active in high wind speeds. The aim of this controller is to limit the output power and rotor speed to their rated values.

When the output power is below its rated value the pitch controller sets the pitch angle equals zero, since it is the optimum value for maximizing the output power. However, when the output power exceeds the rated value the pitch controller increases the pitch angle in order to decrease the performance coefficient and hence decreasing the power captured. Figure 8 shows the block diagram of the pitch angle controller. Since the pitch angle cannot change immediately due to the size of rotor blades, a rate limiter is provided. It limits the rate of change of the pitch angle to  $7^\circ/s$ .

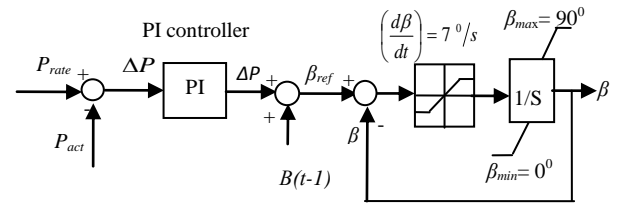


Fig. 8. Block diagram of Pitch Angle Controller.

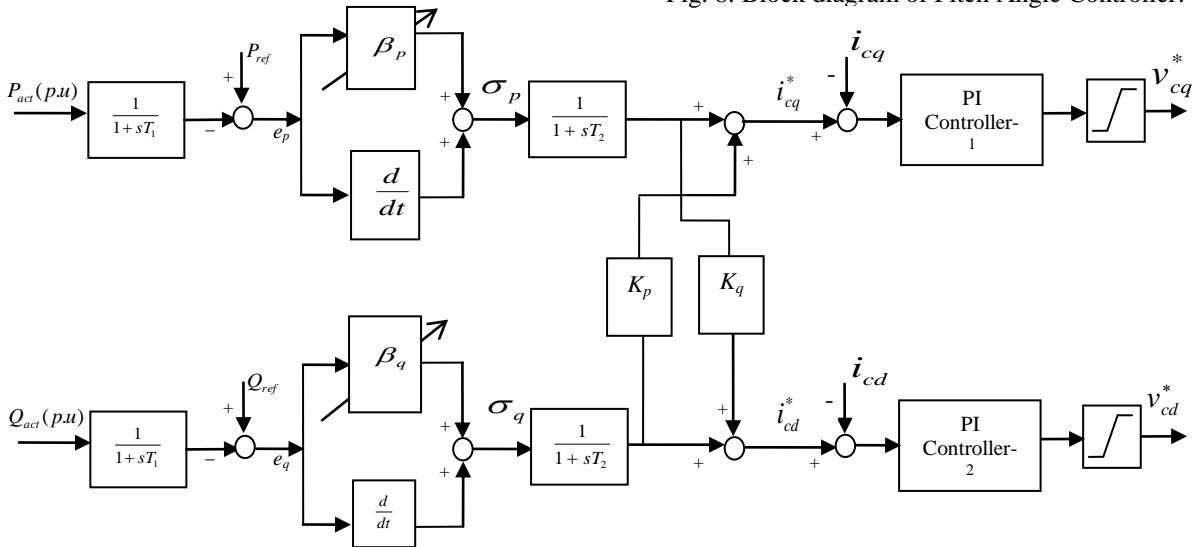


Fig. 5. Novel variable structure coordinated sliding model controller scheme with (P, Q) loop inter-coupling \*

#### 4. DIGITAL SIMULATION RESULTS

The mathematical model of the overall system has been simulated in Matlab-Simulink, with a fixed step solver of fixed step size equals to 0.001sec. The parameters of the wind turbine and the BDFM are given in Appendix B, in addition, the parameters of all controllers used are listed in Appendix C.

Different scenarios are simulated to assess the dynamic performance of both the BDFG controller and the overall control of the variable speed /variable pitch wind turbine. The dynamic response of the system is investigated when the system is subjected to different patterns of wind speed as given in following subsections.

##### 4.1 Digital Simulation Results for Wind Speeds Below its Rated Value

The simulation was carried out when the wind speed had a mean value of 9 m/s with turbulent intensity of 8 % as shown in Figure 9(a). The output active power from the power winding is shown in Figure 9 (b). It can be noticed that the fast oscillations in wind speed are filtered out from the electrical output power.

Figure 9 (c) depicts the generator speed, from which it can be seen that the generator speed follows the reference speed exactly. This assures that the generator is able to extract maximum energy from the wind. It can also be seen that the speed controller has fast response to the changes in wind speed.

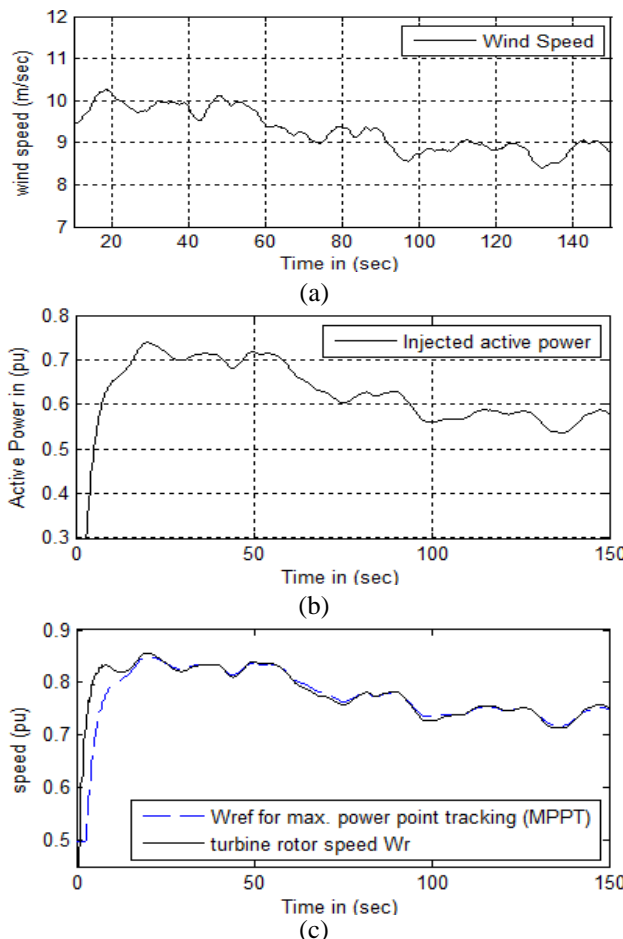


Fig. 9. Wind speed pattern for 150sec. duration (a), injected active power to the grid from the PW (b), rotor speed response and its reference (c)

Figure 10(a) depicts the tip speed ratio (TSR) of the wind turbine; it can be seen that this ratio is approximately equal to the optimal value ( $\lambda_{opt}=6.3$ ). It means that the wind turbine operates at the optimum condition. Figure 10(b) shows the value of the performance coefficient of the wind turbine. It can be noted that its value almost coincides with the optimal value of this turbine which is equal to  $Cp_{max}=0.438$ . Figure 10(c) illustrates the reactive power response and its command, in which the command reactive power was set to zero.

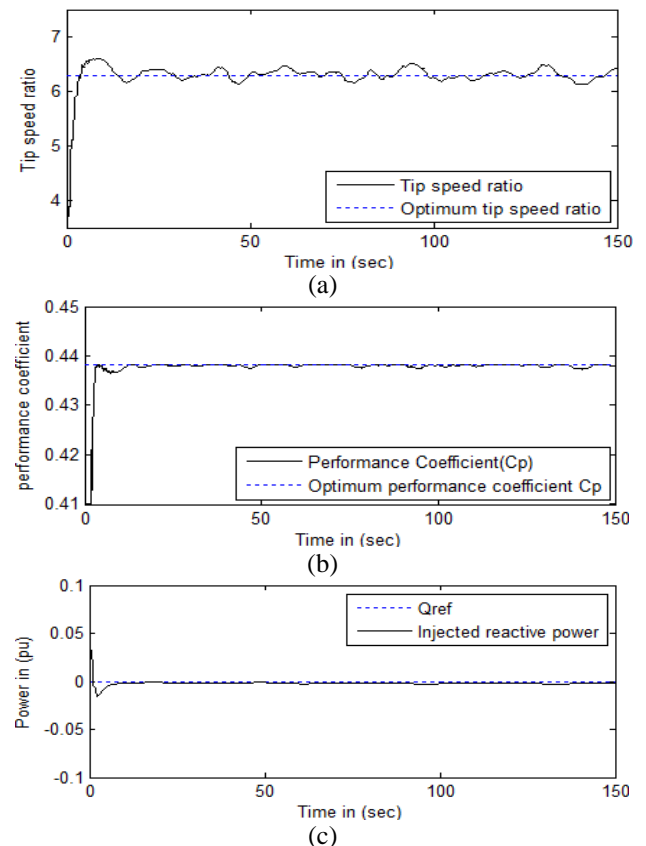


Fig. 10. Tip Speed Ratio of the wind turbine (a), performance coefficient of the wind turbine (b), reactive power response of the PW (c)

##### 4.2 Digital Simulation Results for Wind Speeds around its Rated Value

The simulation was carried out when the wind speed had a mean value of 12 m/s with turbulent intensity of 8 % as shown in Figure 11 (a), (b), (c) illustrate the output active power from the BDFG and the rotor speed respectively. It can be noticed that during the interval, at which the wind speed is larger than its rated value the speed and pitch controllers are active in order to limit the output power and rotor speed to their rated values. On the other hand when the wind speed is smaller than the rated value the speed controller only is active to maximize the output power, but the pitch controller is inactive.

Figure 11 (d) illustrates the pitch angle of the wind turbine blades. It can be seen that the pitch controller was active only in the interval, during which the wind speed is larger than the rated value. Figure 11 (e) illustrates the reactive power response.

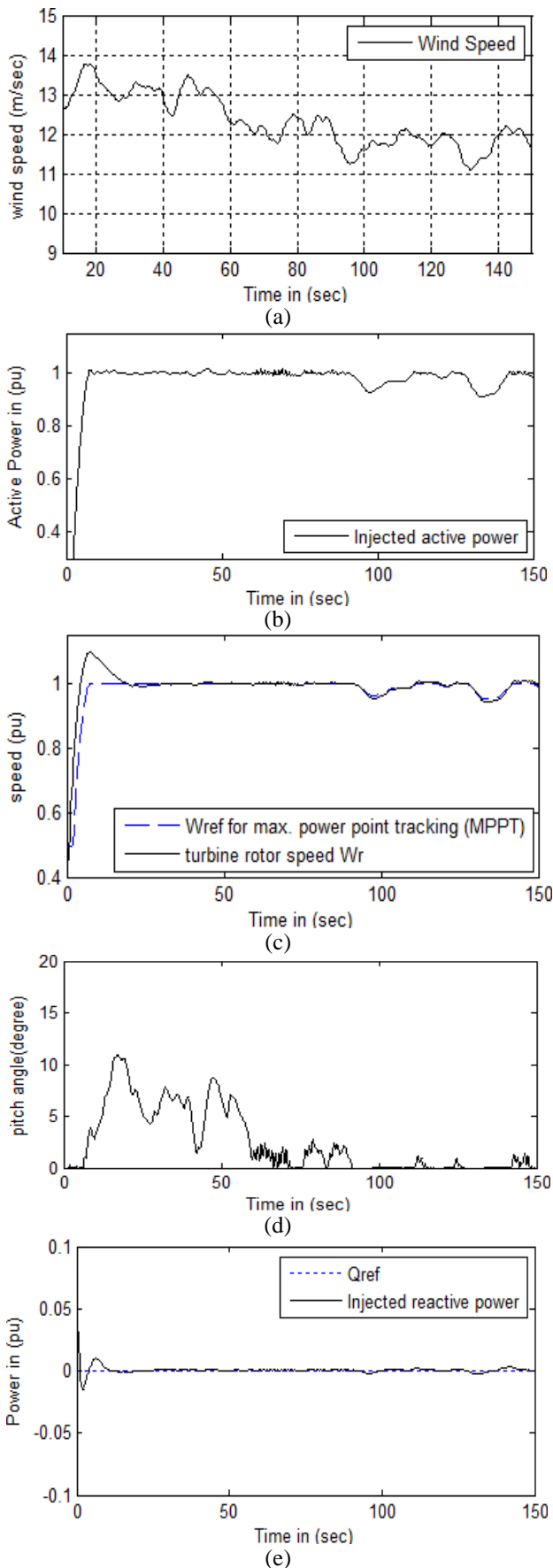


Fig. 11. Wind speed pattern for 150 s. duration (a), injected active power to the grid from the PW (b), rotor speed response and its reference (c), pitch angle (d), reactive power response of the PW (e)

### 4.3 Digital Simulation Results for Step Change of Wind Speed

The simulation results of the system under study are carried out when the system is subjected to a step change in wind speed as shown in Figure 12 (a). Figure 12 (b) depicts the dynamic response of the active power of the power winding, it can be seen that the active power response has a very small overshoot at the instance of step change of wind speed. Figure 12 (c) shows the response of the reactive power. Figure 12 (d) shows the speed response of the rotor, it can be seen that the speed of rotor follow the reference speed with small overshoots at the instance of step change.

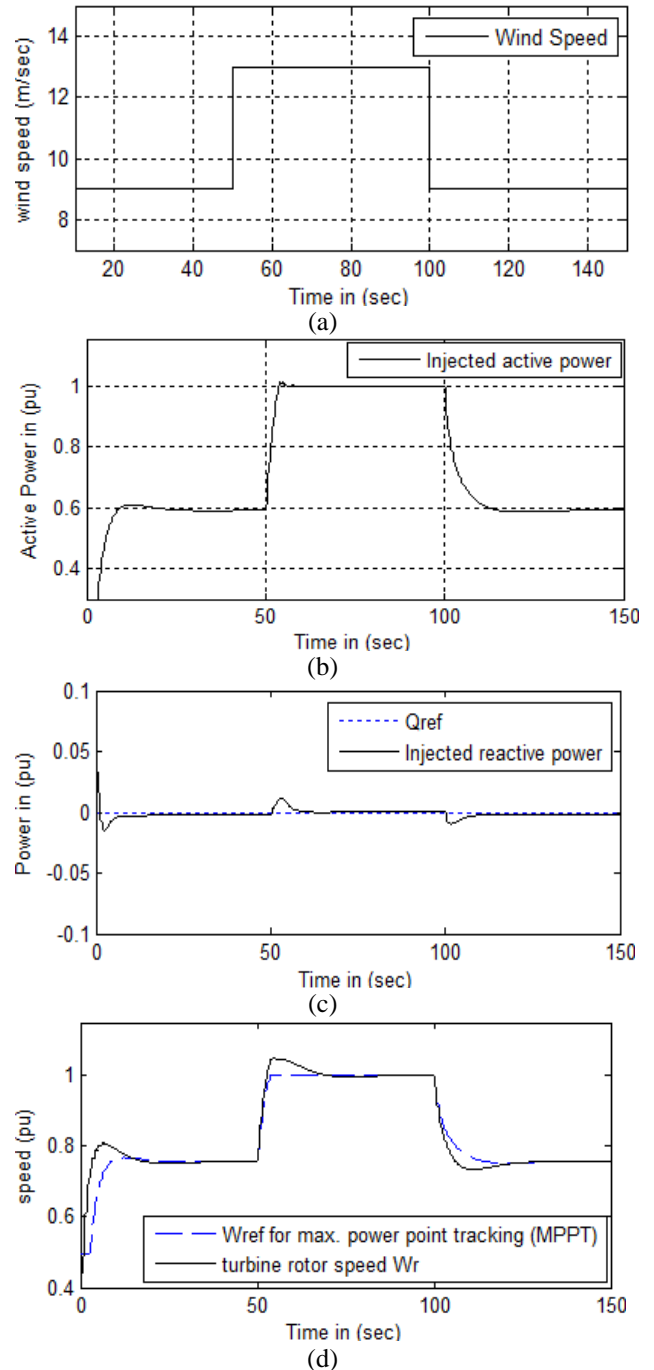


Fig. 12. Wind speed pattern for 150 s. duration (a), injected active power to the grid from the PW (b), reactive power response of the PW (c), rotor speed response and its reference (d).

4.3.1 Digital Simulation Results for Short Circuit Condition

The simulation results of the system under study are carried out when the system is subjected to short circuit at the generator bus. The wind speed was equal to 12 m/s. The output active power from the generator was equal to 1 pu, while the reactive power was equal to zero. The short circuit happened at  $t = 50$  s for duration of 5 cycles (0.1 s) then the fault is cleared.

Figure 13 (a) shows the transient response of the active power output from the power winding of the BDGF. It can be seen that, the power delivered from the BDGF during the fault dropped to zero then after the clearance of the fault it increased to about 1.77 pu, due to the acceleration action, then it is reduced quickly to its steady state value.

Figure 13 (b) depicts the dynamic response of the speed of the wind turbine rotor, it can be seen that at instance of sc occurrence the speed is increased to 1.058 pu, since there is no output power and the input power is absorbed by the rotating parts. Figure 13 (c) shows that the reactive power response is associated with fast oscillations and a 2 pu overshoot then it drops quickly to the same steady state value before the occurrence of the fault.

Figure 13 (d) shows the PW current, it can be seen that the PW current reached 2.1 pu during the fault, then it quickly drops to its steady state value after the clearance of the fault. Figure 13 (e) shows the transient response of the control winding current. It can be seen that this current reached 1.6 pu during the fault.

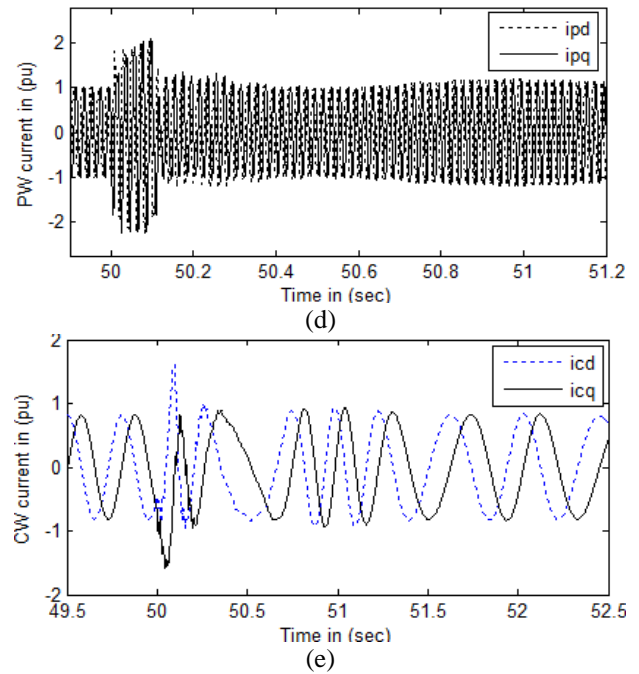
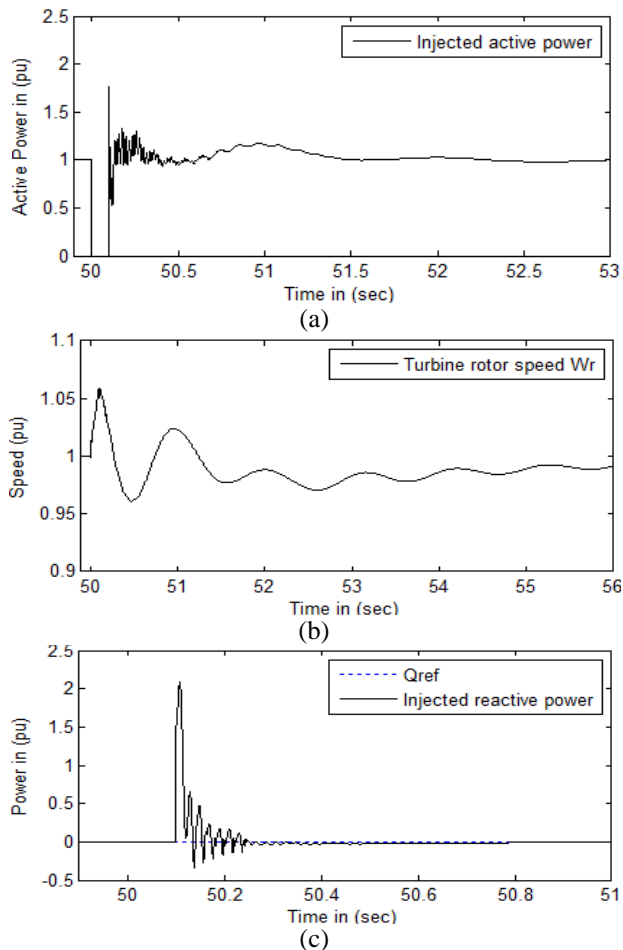


Fig. 13. Output active power from the power winding (a), speed of wind turbine (b), reactive power output from the power winding (c), power winding current in the PW reference frame (d), control winding current (e)

4.3.2 Digital Simulation Results for Open Circuit

The simulation results of the system under study are carried out when the system is subjected to open circuit at the generator bus. The wind speed was constant at 12 m/s, the output active power from the generator was equal to 1 pu, while the reactive power was equal to zero. The open circuit happened at  $t = 50$  s for duration of 2 cycles (0.04 s) then the generator is reconnected to the grid.

Figure 14 (a) shows the active power response of the system, it can be seen that the active power is decreased instantaneously to zero during the open circuit period and at the instance of reconnecting the generator the power is increased with under damped response with maximum overshoot of 0.7 pu, the active power is then reached to steady state value of one pu after 1.5 s.

Figure 14 (b) shows the reactive power response, it can be notice that it has a damped oscillating response with an overshoot of 1.1 pu. Figure 14 (c) depicts the speed response of the wind turbine rotor, it can be notice that at the instance of open circuit the speed is increased to about 1.04 pu, then it oscillate with damped behavior about its rated value, it reached the steady state value after 4 sec. Figure 14 (d) shows the response of the PW currents, it can be seen that the PW current decreased to zero during the open circuit interval then it return to its steady state value quickly after about 1 sec, also it can be noticed that the maximum overshoot of the PW current is 0.8 pu.

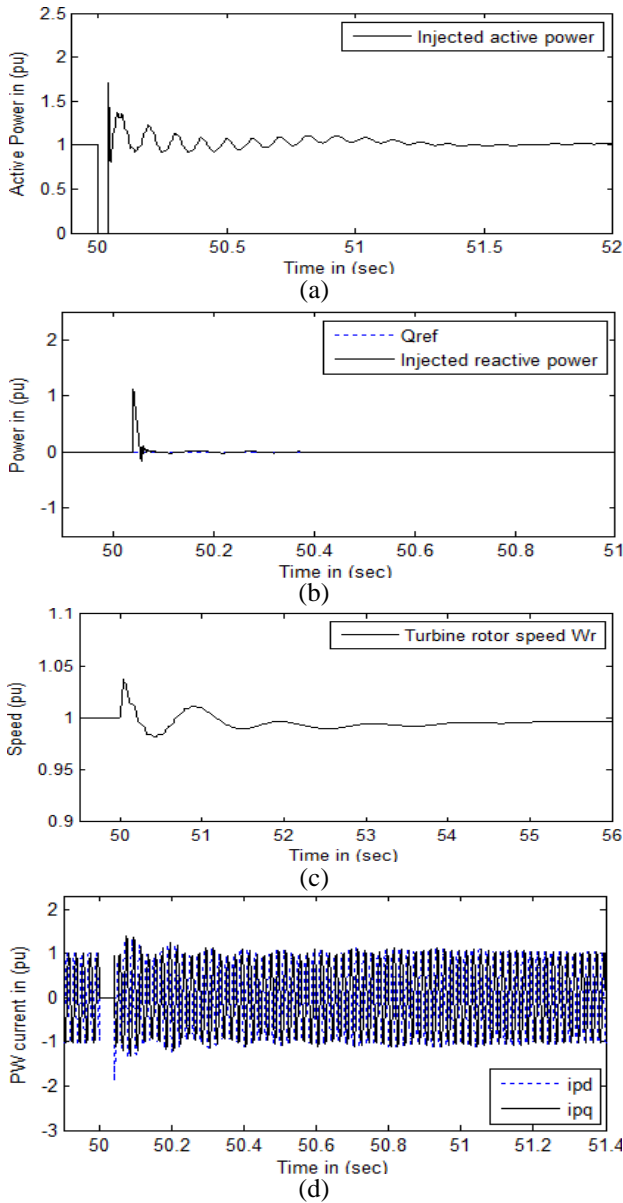


Fig. 14. Output active power from the power winding (a), Reactive power output from the power winding (b), Speed of wind turbine (c), Power winding current in the PW reference frame (d)

## 5. CONCLUSION

This paper presented a new coordinated inter-coupled variable structure controller for the brushless doubly fed induction generator (BDFG) with P, Q loop inter-coupling for the purpose of controlling its active and reactive power. The application of the novel controller for the BDFG machine is validated through simulation analysis on Matlab/Simulink program. The dynamic response of the brushless doubly fed induction generator with this proposed controller is obtained and analyzed. By inspection of the dynamic response, it can be realized that the dynamic response of the BDFG when provided with the proposed controller is improved and the power ripple is minimized in compared with that of the conventional proportional plus integral (PI) controller. The Inter-Coupled controller ensures less ripple content, fast dynamics response and enhanced dynamic fast tracking of power (P, Q) references.

## APPENDICES

### Appendix (A)

Derivation of the dynamic relation between CW and PW current:

Equation (9) can be rearranged as follows:

$$i_r = \frac{\psi_p - L_{sp}i_p}{L_{hp}} \quad (24)$$

Substituting equation (24) into equation (13) to obtain the rotor flux as a function of the PW, the CW currents and the PW flux yields:

$$\psi_r = \frac{L_r\psi_p}{L_{hp}} + (L_{hp} - \frac{L_rL_{sp}}{L_{hp}})i_p + L_{hc}i_c \quad (25)$$

Substituting equations (24) and (25) into equation (12) and putting  $v_r=0$  then expanding the resulting equation into d-q components. Yield equations (19) and (20) which describes the dynamic relation between CW and PW currents.

### Appendix (B)

(i)BDFG data:

$R_{sp}=1.732\Omega$	$R_{sc}=1.079\Omega$	$R_r=0.473\Omega$
$L_{sp}=714.8 \text{ mH}$	$L_{sc}=121.7 \text{ mH}$	$L_r=132.6 \text{ mH}$
$L_{hp}=242.1 \text{ mH}$	$L_{hc}=59.8 \text{ mH}$	$p_1=3$
		$p_2=1$

(ii)The wind turbine data:

Number of blades = 3	Blade radius $R_r = 37.5 \text{ m}$
Turbine inertia (pu) = 2.5 s	Cut in speed = 3 m/s,
Cut out speed = 25 m/s	$\rho = 1.225 \text{ kg/m}^3$ ,
Gear box ratio 1:42	

### Appendix (C)

(i) Parameters of the novel controller:

$T1 = 0.003 \text{ s}$	$T2 = 0.001 \text{ s}$
$\beta_p = 0.7 + 5e_p$	$B_q = 0.78 + 70e_q$
$K_p = 0.1$	$K_i = 0.1$
PI controller -1 $K_p = 40$ , $K_i = 10$ PI controller -1 $K_p = 45$ , $K_i = 25$	

(ii) Parameters of the speed PI controller:

$K_p = 1.8$	$K_i = 0.8$
-------------	-------------

(iii) Parameters of the pitch angle PI controller:

$K_p = 20$	$K_i = 5$
------------	-----------

## References

- [1] A. D. Hansen, F. I. Poul, and F. Blaabjerg, Overall control strategy of variable speed doubly-fed induction generator wind turbine, Nordic wind power conference, 1-2 March, Chalmers University of Technology, (2004).
- [2] R. Pena, J. C. Clar, and G. M. Asher, Doubly fed induction generator using back-to-back PWM converters and its application to variable speed, IEEE Proc. Electr. Power Appl., 143(5), 380-387, (1996).
- [3] K. Protsenko, and D. Xu, Modeling and control of brushless doubly-fed induction generators in wind energy applications, IEEE Trans. Power Electronics, 23(3), 1191-1197, (2008).
- [4] M. S. Boger, A. K. Wallace, R. Spee, and R. Li, General pole number model of the brushless doubly-

- fed machine, IEEE Trans. Ind. Appl., 31(5), 1022-1028, (1995).
- [5] W. R. Brassfield, R. Spee, and T.G. Habetler, Direct torque control for brushless doubly-fed machines, IEEE Trans. Ind. Appl., 32(5), 1098-1104, (1996).
- [6] J. Poza, E. Oyarbide, and D. Roye, New vector control algorithm for brushless doubly-fed machines, Proc. IEEE IECON Conf., Seville, Spain, Vol:2, 1138-1143, November (2002).
- [7] S. O. Madbouly, H. F. Soliman, and A. M. Sharaf, A new coordinated inter-coupled vector control of brushless doubly fed wind driven induction generator, IJPEGT Journal, Issue 2, (2011).
- [8] A. M. Sharaf, W. Wang, and I. H. Altaş, A novel modulated power filter compensator for distribution networks with distributed wind energy, Int. J. Emerg. Electr. Power Syst., 8(3), 1–20, (2007).
- [9] M. E. Şahin, A. M. Sharaf, and H. İ. Okumuş, A novel filter compensation scheme for single phase-self-excited induction generator micro wind generation system, Sci. Res. Essays, 7(34), 3058–72, (2012).
- [10] J.G. Sloopweg, H. Polinder, and W.L. Kling, Representing wind turbine electrical generating systems in fundamental frequency simulations, IEEE Trans. Energy Conversion, 18(4), 516-524, December (2003).
- [11] A. Perdana, O. Carlson, and J. Persson, Dynamic response of grid connected wind turbine with Doubly Fed Induction Generator during disturbances, Nordic Workshop on Power and Industrial Electronics, Trondheim, Norway, (2004).
- [12] S. Heier, Grid integration of wind energy conversion systems, John Wiley & Sons Ltd, (1998).
- [13] Wind Turbine, Implement model of variable pitch wind turbine Matlab/Simulink, website: [www.mathworks.com](http://www.mathworks.com), (2016).
- [14] R. Li, A. Wallace, R. Spee, and Y. Wang, Two-Axis model development of cage-rotor brushless doubly-fed machines, IEEE Trans. Energy Conversion, 6(3), 453-460, September, (1991).
- [15] J. Poza, E. Oyarbide, D. Roye, and M. Rodriguez, Unified reference frame d-q model of the brushless doubly fed machine, IEEE Proc. Electr. Power Appl., 153(5), 726-734, September, (2006).
- [16] R. Carlson, H. Voltolini, F. Runcos, P. Kuo-Peng, and N. J. Batistela, Performance analysis with power factor compensation of a 75 kw brushless doubly fed induction generator prototype, Proc. IEEE IEMDC Conf., Antalya, Turkey, vol:2, 1502-1507, May, (2007).
- [17] D. Basic, J. G. Zhu, G. Boardman, Transient performance study of a brushless doubly fed twin stator induction generator, IEEE Trans. Energy Conversion, 18(3), 400-408, September (2003).

## Biographies



**Dr. Sayed O. Madbouly** is currently an assistant professor at Electric Power and Machines Department, Faculty of Engineering, Ain Shams University. He was born in Cairo, Egypt on November 28, 1975. He received his B.Sc., M.Sc. and Ph.D. degrees in Electrical Engineering from Electrical Power and Machines Department, Faculty of Engineering, Ain Shams University, Cairo, Egypt, in 1998, 2004 and 2010 respectively. His current Research areas include Electric Drives, Renewable Energy, and Artificial Intelligent Applications on Electrical Machines.

E-mail: [sayed\\_madbouly@hotmail.com](mailto:sayed_madbouly@hotmail.com)



**Prof. Adel M. Sharaf** obtained his B.Sc. degree in Electrical Engineering from Cairo University in 1971. He completed an M.Sc degree in Electrical engineering in 1976 and Ph.D degree in 1979 from the University of Manitoba, Canada and was employed by Manitoba Hydro as Special Studies Engineer, responsible for engineering and economic feasibility studies in Electrical Distribution System Planning and Expansion. Prof. Sharaf was selected as NSERC-Canada research-assistant professor in 1980 at University of Manitoba. He joined the University of New Brunswick in 1981 to start a tenure-track academic career as an Assistant professor and he was promoted to Associate Professor in 1983, awarded tenure in 1986, and the full professorship in 1987. Dr. Sharaf has extensive industrial and consulting experience with Electric Utilities in Canada and Abroad.

E-mail: [profdramsharaf@yahoo.ca](mailto:profdramsharaf@yahoo.ca)

# Electromagnetic Radiation Measurement of a High Power Wireless Network Adapter

Yasin Karan<sup>1,\*</sup>, Nilüfer As<sup>1</sup>

<sup>1</sup>Department of Physics, Recep Tayyip Erdoğan University, Rize, 53100, Turkey

Received: 1 August 2016; Revised: 5 September 2016 Accepted: 10 September 2016; Published: 1 December 2016

Turk J Electrom Energ Vol.: 1 No: 2 Page: 17-23 (2016)

SLOI: <http://www.sloi.org/>

\*Correspondence E-mail: [yasin.karan@erdogan.edu.tr](mailto:yasin.karan@erdogan.edu.tr)

**ABSTRACT** Electromagnetic pollution is an active research area, especially after the widespread deployment of Global System for Mobile Communications (GSM) base stations in the environment. Numerous studies on electromagnetic pollution of base stations are available in literature. Health effects of GSM base station and signals are engrossing and researches in this field have been going on. In this particular study, electromagnetic radiation (EMR) of wireless network adapters with high gain antenna is analyzed and compared with other electromagnetic radiation sources. The measurements are realized in long and short distances from the transmitter. The results indicate that the high power wireless network adapter radiation is significantly higher than the other electromagnetic sources in residential environment, especially compared with GSM signals and common wireless network adapters.

**Keywords:** Wireless network adapter, Electromagnetic radiation, Electromagnetic pollution, IEEE 802.11 standard, Selective radiation measurement.

**Cite this article:** Y. Karan, N. As, Electromagnetic Radiation Measurement of a High Power Wireless Network Adapter, Turkish Journal of Electromechanics & Energy 1(2) 17-23 (2016)

## 1. INTRODUCTION

The base stations came into our lives with GSM technology development in the beginning of 1990s. That caused the public to worry about the electromagnetic pollution radiated from cell phones, base stations especially close to their home and also TV/Radio transceivers. The limitations of the emitted power are regulated by related authorities. Nevertheless, today almost every home has its own electromagnetic sources which are wireless network routers and adapters.

There have been many studies about measurement of electromagnetic radiation [1-10]. The electric field strength level in the schools, hospitals, dormitories, residences and high towers around city center of Ankara was measured 1.64 V/m (max.) with a mean of 0.32 V/m, and standard deviation of 0.255 V/m in GSM frequency bands [2]. The electric field strength of base stations in the city of Nablus, Palestine was measured in different distances and the maximum value was found to be 3.49 V/m at 10 m distance [3]. In another study, electromagnetic field exposure level of main streets in Diyarbakır city was analyzed statistically and it is seen that the results are not in normal distribution [4]. A base station in Rize, Turkey was measured and

maximum 1.114 V/m in terms of electric field strength and 3.248 mW/m<sup>2</sup> in terms of power density were found in [5-7]. 60 base stations measurements were carried out in Australia and the maximum power density value was found to be 7.8 mW/m<sup>2</sup> [8].

In another study, electromagnetic field strengths in different European cities were investigated and it was found to be below the International Commission on Non-Ionizing Radiation Protection (ICNIRP) limit values [9]. TV/Radio transmitter towers in Trabzon city were investigated in terms of electric field and it was found that the maximum value was 0.4732 V/m in FM band [10]. In a different approach to base stations, the  $\gamma$  radiation dose levels were measured with the samples taken from different distances from a base station, and the results showed a higher value in the base station environment compared to the non-base station environment [11]. The simulation and real environment measurements of electromagnetic propagation for Wi-Fi access points were compared and 3 dB differences were found in [12].

The effect of electromagnetic field on human health was also studied by several researchers. For example,

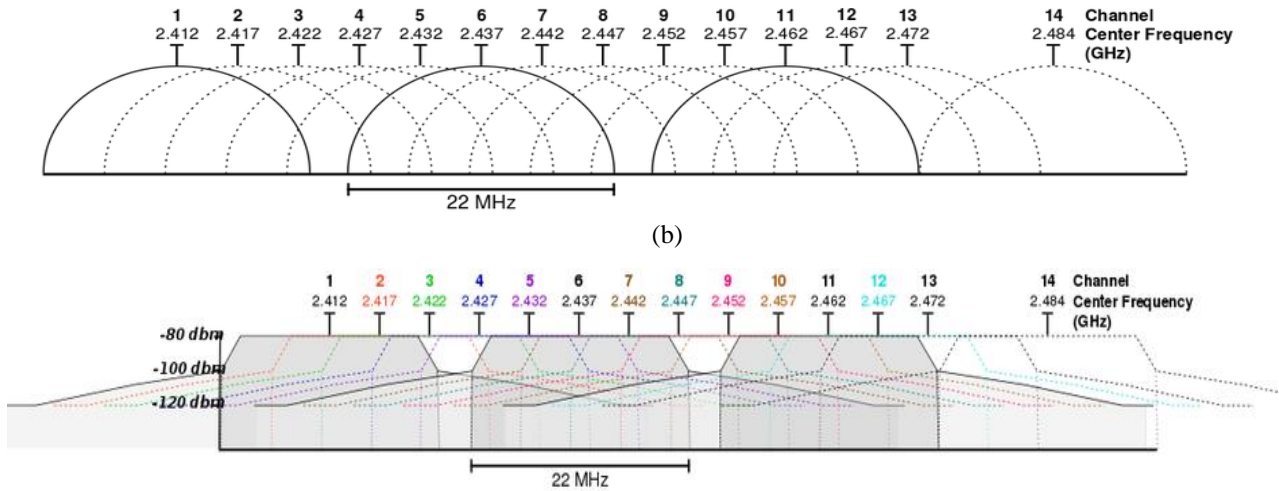


Fig. 1. Channel specifications in IEEE 802.11 standard (a) channels frequency bands, (b) channels power figure [16]

variation of temperature around human ear and head exposed to electromagnetic radiation was analyzed in another study. It was noted that electromagnetic field effect using cell phone resulted in temperature change of 0.22 - 0.39 °C on ear and 0.07 - 0.17 °C on head [13]. The effect of 900 MHz electromagnetic field on cortisol and testosterone level was analyzed to examine the effect of Electromagnetic Radiation (EMR) on organic tissues. The rats were exposed to electromagnetic wave of 1 mW/cm<sup>2</sup> for 30 min/day in 4 weeks. Consequently, cortisol values were found higher and the testosterone level was lower in the rats exposed to electromagnetic field compared to the electromagnetic free rats [14].

In our study, the electric field strength of a wireless network adapter for wireless local area network (WLAN) is investigated. In the literature, while experimental data for GSM base stations and TV-radio transmitters is present, no experimental data for the wireless network adapter for WLAN especially with high gain antenna is available yet. Since the internet usage has expanded in all environments and accessing to internet service has certain cost, some people tend to access free internet from public internet suppliers even from long distance. In order to do that, a high power wireless network adapter with high gain antenna can be used to have long distance communication without considering the electromagnetic field strength of the device. In this study, the electric field strength of a high power wireless network adapter was measured by internet usage and transmission distance. The results were compared with other wireless systems and with random network adapters.

1.1 IEEE 802.11 Standard

IEEE 802.11 is wireless local area network standard published by IEEE community. This standard includes the media access control (MAC) layer and Physical layer properties of the WLAN. Industrial, Scientific and Medical (ISM) radio frequency bands are used in IEEE 802.11 standard. ISM bands are the reserved radio bands for public use. IEEE 802.11 has some types named as IEEE 802.11x where x is a, b, g, n, ac, ad, etc. for different types. These types are differentiated mainly by frequency, data rate and modulation type. While IEEE

802.11a uses 5 GHz ISM band, b and g use 2.4 GHz ISM band, and n uses both 2.4 and 5 GHz bands.

In Turkey, where the experiments carried out, only 2.4 GHz band is allowed to be used for WLAN. Therefore, 802.11 b/g/n standards are allowed to be used in Turkey. These standards have 14 channels. These 14 channels are shown in Figure 1 (a) with central frequencies. The bandwidth of each channel is 22 MHz and each channel is 5 MHz apart from the next channel except the 14<sup>th</sup> one. This channel is 12 MHz apart from the previous channel. As seen in the Figure 1, adjacent channels are interfering with each other. Because of that, non-interfering channels should be used for the same time to avoid the interference. The channels 1, 6 and 11 or the channels 2, 8 and 11 can be used at the same time. The 14<sup>th</sup> channel is restricted by many countries and the channels 12 and 13 can be used with a lower power according to the some country regulations [15].

Figure 1 (b) shows the spectral mask of IEEE 802.11 channels. For a reliable data transfer, each channel needs to be attenuated at least 20 dB from central frequency power in the edge frequencies.

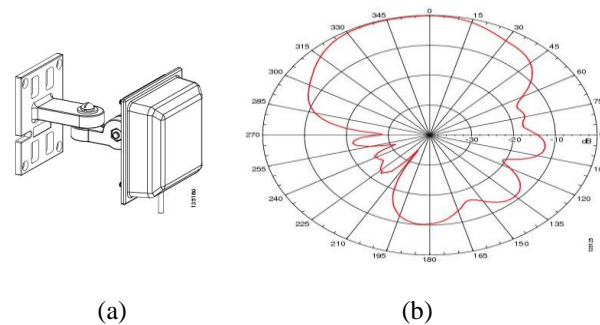


Fig. 2. (a) Cisco AIR-ANTM5560P-R Antenna, (b) its E-field radiation pattern (Cisco guideline, Cisco Multiband Wall-Mount Antenna (AIR-ANTM5560P-R)", 2007)

Antennas are used to radiate and capture RF energy with some gain. Directional antennas radiate and capture more power in a specific direction. Therefore, its radiation pattern shows higher power in some direction and a lower power in other directions, while omnidirectional antenna pattern shows equal power in every direction in one plane. Figure 2 (a) shows an example of a directional antenna and its radiation pattern. As in the Figure 2 (b),

the frontal area has more coverage (power) than other sides. The wireless network adapter that was used in the experiment has a directional antenna.

1.2 ICNIRP and ICTA Standard

The maximum limit values of exposure to electromagnetic field are imposed by country regulators. The International Commission on Non-Ionizing Radiation Protection (ICNIRP), an independent organization, sets the limits and updates them. Most of the countries set their rules based on ICNIRP limits. For instance, the limits in Turkey were quarter of the ICNIRP limits. With last updates, now, the limits are even lower than the quarter of ICNIRP limits. The Information and Communication Technologies Authority (ICTA) is a legal institution in Turkey and it is responsible for deciding the limit values of electromagnetic exposure values. These limits differ due to occupational exposure and public exposure. Occupational exposure limits are kept higher than public exposure limits. Table 1 shows the limit values of ICNIRP and ICTA for electric field, magnetic field and power density [17-19]. Electromagnetic field strength limits of ICTA were updated in 2015 [19].

Table 1. Reference levels for general public exposure to time-varying electric and magnetic fields

Frequency range (MHz)	E-field strength (V/m)		H-field strength (A/m)	
	ICNIRP	ICTA	ICNIRP	ICTA
400–2000	$1.375f^{1/2}$	$0.305f^{1/2}$	$0.0037f^{1/2}$	$0.00082f^{1/2}$
900	41.25	9.15	0.111	0.0246
1800	58.34	12.94	0.157	0.0348
2000-60000	61	13.5	0.16	0.035

Additional to E-field strength limitations, ICNIRP defines Specific Absorption Rate (SAR) limits. SAR is the absorbed amount of electromagnetic energy per kg by a normal human body. SAR is proportional with E-field strength. Mobile phones use SAR values as E-field limitations. The calculation of SAR is simplified by the equation;

$$SAR = \sigma E^2 / \rho \tag{1}$$

where  $\sigma$  is conductivity in  $S/m$ ,  $E$  is electric field in  $V/m$  and  $\rho$  is density in  $W/kg$  [17]. As seen in Equation 1, SAR is related with conductivity and density of human body or tissue. Since conductivity and density of tissue are flexible, obtaining precise SAR value is not feasible.

2. EXPERIMENTAL

In the experimental setup, the wireless network adapter is in a 10-story apartment flat and 180 meter away from an access point which is located in a university campus. From this distance, it is not possible to make a reliable connection and access to internet with a common wireless network adapter. However, the connection can be successfully made with high

power 802.11b/g network adapter which is equipped with a high gain directional antenna.

Figure 3 shows the measurement point (access point shown as ‘‘AP’’) and the network adapter place (red dot). As seen in the figure, the distance is roughly 180 m. Also there are obstacles between them such as two apartment corners, walls and windows. These obstacles attenuate, reflect and scatter the electromagnetic waves and that have a bad influence on reliable wireless communication. When there is line of sight (LOS) between transmitter and receiver, wireless communication can be successful in longer distances, compared to when there is non-line of sight (nLOS). The wireless network adapter is inside of the apartment as seen in Figure 4 (a). Figure 4 (b) shows the measurement points around the antenna. The antenna and network adapter were chosen as high gain and powered. Those devices are OEM (Original Equipment Manufacturer) devices and commonly available in electronics markets.

Electromagnetic field measurements were realized with a compact spectrum analyzer device (SRM 3006, Narda Safety Test Solutions GmbH, Pfullingen, Germany). It measures the electric field in the 420 MHz- 6 GHz frequency range with a triaxial coil antenna. Electric field can be converted to both magnetic field and power flux density values using Equation 2 and 3 assuming in far field measurement. The measurement results were recorded in the device and uploaded to a computer using its software [5].

$$\mathbf{E} = \eta_0 \mathbf{H} \tag{2}$$

$$\mathbf{S} = \mathbf{E} \times \mathbf{H} \tag{3}$$

where  $E$  is electric field strength in  $V/m$ ,  $\eta_0$  is free-space impedance equal to  $377 \Omega$ ,  $H$  is magnetic field strength in  $A/m$ ,  $S$  is power flux density in  $W/m^2$ .



Fig. 3. The measurement point and with roughly distance; AP and Red dot are the access point and measured antenna locations

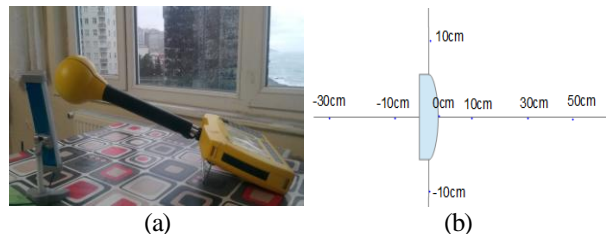


Fig. 4 (a) Measured antenna and measurement view. (b) The measurement points around measured antenna

**3. RESULTS**

The results are given based on distance between the access point and the wireless network adapter: in-campus and off-campus and in case of the internet usage: active-use and passive-use parts. The distance between access point and the adapter is short in in-campus measurements and long in off-campus measurements. There was continuously file downloading and video streaming in the active-use, however there was not any file downloading but just internet surfing in passive-use. The transmitted power and duration vary due to the transmission distance and usage. The measurement points are kept in a short distance from the antenna because wireless network adapter antennas are used as attached to computer, so they can be next to human body.

Table 2. The electric field strengths (V/m) of measured points

Distance (cm)	Off-campus active-use		Off-campus passive-use		In-campus active-use		Home Wi-Fi router active-use	
	Max. peak	Max. mean	Max. peak	Max. mean	Max. peak	Max. mean	Max. peak	Max. mean
-120	0.20	0.03	-	-	-	-	-	-
-100	-	-	-	-	-	-	1.49	0.08
-50	0.53	0.07	-	-	0.38	0.02	-	-
-30	1.01	0.18	-	-	0.55	0.03	2.99	0.12
0	11.8	1.61	5.45	0.17	5.62	0.24	3.39	0.20
10	9.77	1.11	5.49	0.15	-	-	-	-
20	-	-	-	-	4.38	0.19	0.72	0.11
30	3.67	0.60	2.71	0.06	-	-	-	-
50	2.19	0.35	1.61	0.04	2.66	0.09	0.65	0.08
70	0.99	0.17	0.79	0.02	1.31	0.07	0.79	0.06

Table 2 shows the results of all measurements cases. At long distance, both active and passive usages were investigated and the results are shown as off-campus active-use and off-campus passive-use in Table 2. By using the same wireless network adapter, another measurement was realized in the campus where the access point is close to the network adapter. The results of in-campus measurements are given in in-campus active-use part of Table 2. Another measurement was carried out in a house with a common use wireless network router. The measurements were carried out at different times and measurement distances could vary in each experiment. Therefore, only measured data and distances were given in the table.

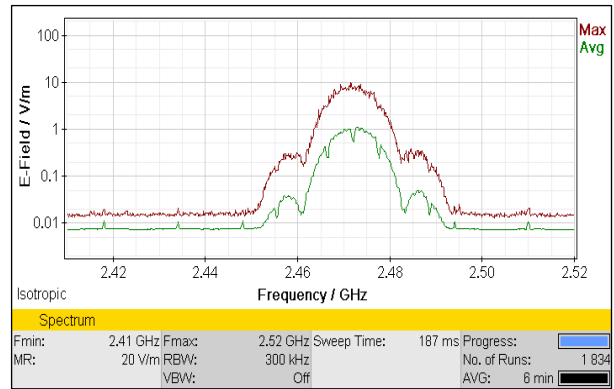
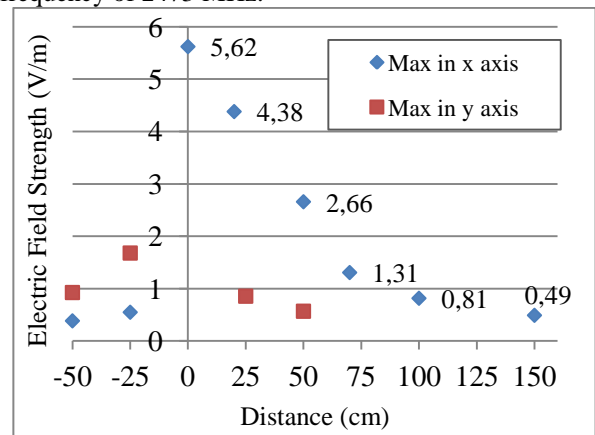
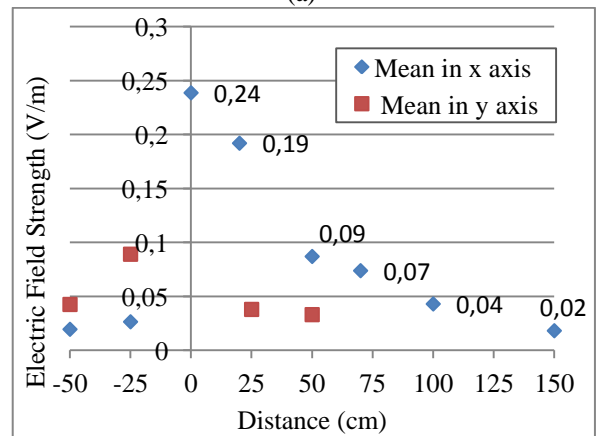


Fig. 5. One of the throughputs from spectrum analyzer in the measurement of out of campus active used at 10 cm distance

Figure 5 shows one of throughput of the spectrum analyzer measurements. It is the electric field strength in the 2.4 - 2.52 GHz band at 10 cm distance from directional antenna in the out of campus active downloading usage. The center frequency seems 2.472 GHz, so the channel number of this channel is 13 as seen in Figure 1 (b). Maximum electric field strength is 9.77 V/m in the frequency of 2471.6 MHz. Among the average values, the maximum average value is 1.11 V/m in the frequency of 2473 MHz.



(a)



(b)

Fig. 6. (a) The maximum peak and (b) the maximum of mean values of electric field strength values in two directions for in-campus active-use

Figure 6 (a) and (b) show the maximum peak of electric field strength and maximum mean values in the 2.4-2.5 GHz range for in-campus active-use, respectively. In both figures, antenna is measured in x and y directions as shown in Figure 4 (b). Since the antenna is directional, the electric field strength is lower in the lateral and back side than the front side of the antenna. The same measurement was performed in off-campus measurement, and similar results; lower intensity in the back and lateral side than the front side were obtained as expected. The data in Figure 6 (a) shows the maximum peak values of measurements in the 2.4 - 2.5 GHz band while the data in the Figure 6 (b) shows the maximum value of the mean values of the same measurements. Each measurement was realized in at least six minutes time interval.

Figure 7 compares the maximum electric field strengths of four measurements and Figure 8 compares the maximum mean values of electric field strengths of four measurements. These data can also be seen in Table 2. Both figures show that the electric field is the highest in off-campus measurements when there is a continuous downloading. Its values are fairly higher than the others especially in maximum of mean values. When there is not continuous downloading in off-campus measurements, the electric field strength is less than the continuous downloading in-campus measurements. The home measurements with a common router showed the minimum electric field strength among the continuous downloading measurements. Also, since its antenna is not directional, the electric field is similar in positive and negative directions. As expected, the electric field strength gets lower with the increasing distance except in the last data of home measurement with the common wireless router. The reason of this data is that the second wireless receiver (computer) started to access to the router and began downloading a file at that time.

If the results of these measurements are compared with the references given in the introduction, it can be interpreted that the electric field strength of high gain antenna in wireless adapters is more dominant than the base stations, because they are closer to human body. In

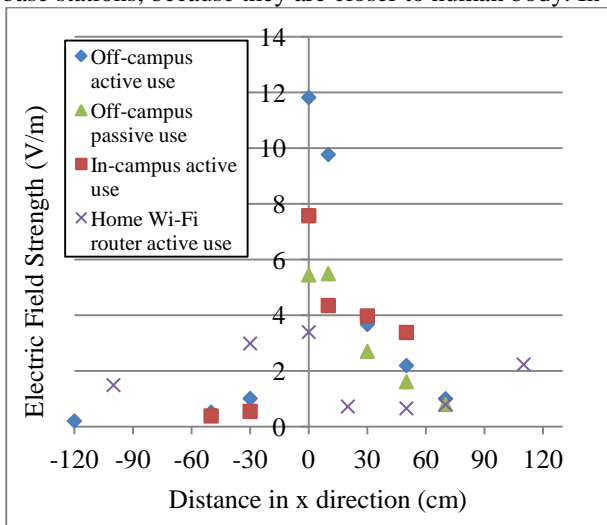


Fig. 7. The maximum electric field strengths in four measurements

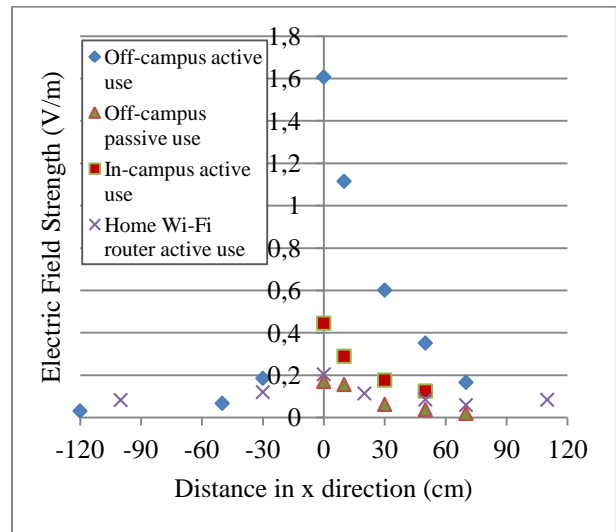


Fig. 8. The maximum mean values of electric field strengths in four measurements

this study, measured electric field strength values are much higher than the measured electric field strength values in references, even the measurements are realized in residential environment. Since WLAN adapter's antennas could be located inside of a room and close to the users, near and far field of the antenna was measured. These high power adapters can be used to access to WLAN routers at long distances. Nonetheless, since the measurements of high power adapters showed much higher EMR than the common wireless router, it is suggested locating the antenna outside the room.

In Figure 9, 700 MHz – 2.5 GHz band was measured, as well when there is a phone calling and the phone was next to the spectrum analyzer; also the spectrum analyzer was 10 cm away from the directional antenna of the wireless network adapter. Additionally, the mobile operator used in the measurement uses the 1800 MHz band. From the figure, it is seen that the electric field strength of wireless network adapter is much higher than other active bands. Especially, when mean powers of EM sources are compared, wireless network adapter is multiple times higher than other sources.

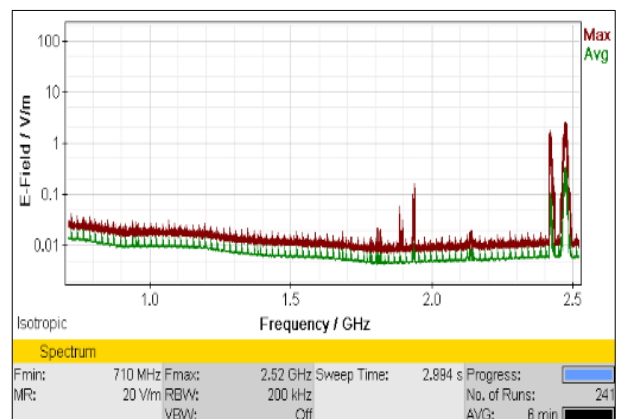


Fig. 9. A general view of the spectrum when there is a cell-phone calling and wireless internet usage (the measurement distance is 10 cm)

#### 4. CONCLUSION

In this study, the electromagnetic pollution of the wireless network adapter with a high gain antenna in long distance was analyzed in terms of electric field strength. The measurements were realized in short distance and long distance from WLAN access point during continuous downloading and no downloading. Also, one of the common used wireless router's electric field strength was measured to compare with a network adapter. The result showed the wireless network adapter with high gain causes considerably more electromagnetic pollution compared to the standard home wireless router because of the transmission in longer distance. Also, when the distance between transceivers is getting longer, emitted electromagnetic signal strength increases. The amount of the difference is significant around the antenna. Therefore, high gain wireless antenna of wireless network adapters or router is better to be kept out of the rooms. At least, it is better to be kept the antenna in longer distance from human body. By comparing measured EMR with the limitations of ICNIRP and ICTA regulations, those are below, yet close to the ICTA limitation values in some cases. Also, the overall results showed that EMR of wireless adapters and routers is higher than the base-stations' EMR given in the references, because base-station antennas are far from human active life, but adapters and routers are close. Thus, it is better to use them cautiously.

#### References

- [1] B.O. Ayinmode, I.P. Farai, Measurement and Method in Radiofrequency Radiation Exposure Assessments, *The Pacific Journal of Science and Technology*, 14, 110-118 (2013).
- [2] O. Genc, M. Bayrak, E. Yaldiz, Analysis of the effects of GSM bands to the electromagnetic pollution in the RF spectrum, *Progress in Electromagnetics Research*, 101, 17-32 (2010).
- [3] A. Mousa, Electromagnetic radiation measurements and safety issues of some cellular base stations in Nablus, *Journal of Engineering Science and Technology Review*, 4(1), 35-42, (2011).
- [4] M. Cansiz, T. Abbasov, M.B. Kurt, A.R. Celik, Mobile measurement of radiofrequency electromagnetic field exposure level and statistical analysis, *Measurement*, 86, 159-164, (2016).
- [5] M.E. Sahin, N. As, Y. Karan, Selective Radiation Measurement for Safety Evaluation on Base Stations, *Gazi University Journal of Science*, 26(1), 73-83, (2013).
- [6] M.E. Sahin, Y. Karan, N. As, Spectrum analyzer measurement technique for safety evaluation on wireless communication systems, In 30th URSI 2011 General Assembly and Scientific Symposium; August 13-15, Istanbul, Turkey, 1-4, (2011).
- [7] N. As, B. Dilek, M. E. Şahin, Y. Karan, Electromagnetic pollution measurement in the RTE university campus area, *Global Journal on Advances in Pure & Applied Sciences*, 3, 65-72, (2014).
- [8] S.I. Henderson, M.J. Bangay, Survey of RF exposure levels from mobile telephone base stations in Australia, *Bioelectromagnetics Journal*, 27(1), 73-76, (2013).
- [9] D. Urbinello, W. Joseph, A Huss, L. Verloock, J. Beekhuizen, R. Vermeulen, L. Martens, M. Röösl, Radio-frequency electromagnetic field (RF-EMF) exposure levels in different European outdoor urban environments in comparison with regulatory limits, *Environ Int.*, 68, 49-54, (2014).
- [10] E. Eyüboğlu, H. Kaya, Measurement of TV/radio transmitters at Trabzon-Boztepe region induced electric field strength and evaluation of results, In: *Electrical, Electronics and Computer Engineering (ELECO) 2010 National Conference*, Bursa, Turkey. 459-462, December (2010).
- [11] I. Akkurt, B. Mavi, The measurement of radiation dose around base-stations, *Sci Res Essays*, 5(15), 2088-2090, (2010).
- [12] M. Elsayed, A.F. Abdelazid, M. Hasna, D. Trincherro, Exposure assessment to WiFi access points by simulations and measurements, In *Conference Electromagnetics in Advanced Applications (ICEAA) International*, Torino, Italy, 1442-1445, 12-15 September (2011).
- [13] M.R. Faruque, N. Misran, R. Nordin, M.T Islam, B. Yatim, Estimation of specific absorption rate and temperature increases in the human head due to portable telephones, *Sci Res Essays*, 6(6), 1209-1215, (2011).
- [14] A. Koyu, G. Cesur, F. Özgüner, O. Elmas, Effect of 900 MHz electromagnetic field emitted from cellular phone on serum cortisol and testosterone level, *SDÜ Tıp Fakültesi Dergisi*, 12(1), 52-56, (2005).
- [15] IEEE Computer Society LAN MAN Standards Committee, Wireless LAN medium access control (MAC) and physical layer (PHY) specifications, *IEEE Standard*, 802(11), 2012.
- [16] "2.4\_GHz\_Wi-Fi\_channels (802.11b,g\_WLAN)" by Michael Gauthier is licensed under Creative Commons Attribution-Share Alike 3.0 Unported license.
- [17] Guideline IC, Guidelines for limiting exposure to time-varying electric, magnetic, and electromagnetic fields (up to 300 GHz), *Health Phys*, 74(4), 494-522, (1998).
- [18] Başbakanlık Mevzuatı Geliştirme ve Yayın Genel Müdürlüğü Bilgi Teknolojileri ve İletişim Kurumu, Elektronik Haberleşme Cihazlarından Kaynaklanan Elektromanyetik Alan Şiddetinin Uluslararası Standartlara Göre Maruziyet Limit Değerlerinin Belirlenmesi, Kontrolü ve Denetimi Hakkında Yönetmelik, R.G. 2011; Sayı: 27912.
- [19] Başbakanlık Mevzuatı Geliştirme ve Yayın Genel Müdürlüğü Bilgi Teknolojileri ve İletişim Kurumu, Elektronik Haberleşme Cihazlarından Kaynaklanan Elektromanyetik Alan Şiddetinin Uluslararası Standartlara Göre Maruziyet Limit Değerlerinin Belirlenmesi, Kontrolü ve Denetimi Hakkında Yönetmelikte Değişiklik Yapılmasına Dair Yönetmelik, R. G. 2015; Sayı: 29497.

## Biographies



**Yasin KARAN** was born in Istanbul, Turkey. He received his B.Sc. degree in Electronics and Communication Engineering from Kocaeli University, M.Sc. degree from University of Rochester, NY, USA in 2006 and 2009, respectively. He is currently

continuing his doctoral studies at Karadeniz Technical University. He is currently a lecturer in Physics Department at RTE University. His main research interests are wireless communication, microcontroller systems.

E-mail: [yasinkaran@gmail.com](mailto:yasinkaran@gmail.com)



**Nilüfer AS** was born in 1970 in Çanakkale, Turkey. She received her B.Sc. degree, M.Sc. degree, Ph.D. degree in Physics from Uludağ University (U.U.), Bursa, Turkey in 1992, 1994 and 2002, respectively. She is currently an Assistant Professor in

Physics Department at RTE University. She was worked Faraday Effect, Electromagnetic Wave Analysis in Fiber Wave Guides, Non-Ionizing Electromagnetic fields measurements and several topics in the field of General Physics. She was worked at different projects on Solid State Physics, Nuclear Physics and General Physics areas. She has been a member of Turkish Physical Society (TFD). She is currently manager of RTE University Electromagnetic Pollution Center.

E-mail: [nilufer.as@erdogan.edu.tr](mailto:nilufer.as@erdogan.edu.tr)